

RAISHIN: A High-Resolution Three-Dimensional General Relativistic Magnetohydrodynamics Code

Yosuke Mizuno^{1 6}, Ken-Ichi Nishikawa^{1 2}, Shinji Koide³, Philip Hardee⁴
and Gerald J. Fishman⁵

ABSTRACT

We have developed a new three-dimensional general relativistic magnetohydrodynamic (GRMHD) code, RAISHIN, using a conservative, high resolution shock-capturing scheme. The numerical fluxes are calculated using the Harten, Lax, & van Leer (HLL) approximate Riemann solver scheme. The flux-interpolated, constrained transport scheme is used to maintain a divergence-free magnetic field. In order to examine the numerical accuracy and the numerical efficiency, the code uses four different reconstruction methods: piecewise linear methods with Minmod and MC slope-limiter function, convex essentially non-oscillatory (CENO) method, and piecewise parabolic method (PPM) using multistep TVD Runge-Kutta time advance methods with second and third-order time accuracy. We describe code performance on an extensive set of test problems in both special and general relativity. Our new GRMHD code has proven to be accurate in second order and has successfully passed with all tests performed, including highly relativistic and magnetized cases in both special and general relativity.

Subject headings: accretion, accretion disks - black hole physics - magnetohydrodynamics: (MHD) - method: numerical -relativity

¹National Space Science and Technology Center, 320 Sparkman Drive, VP 62, Huntsville, AL 35805, USA; Yosuke.Mizuno@msfc.nasa.gov

²Center for Space Plasma and Aeronomic Research, University of Alabama in Huntsville

³Department of Physics, Kumamoto University, Kurokami, Kumamoto, 860-8555, Japan

⁴Department of Physics and Astronomy, The University of Alabama, Tuscaloosa, AL 35487, USA

⁵NASA-Marshall Space Flight Center, National Space Science and Technology Center, 320 Sparkman Drive, VP 62, Huntsville, AL 35805, USA

⁶NASA Postdoctoral Program Fellow/ NASA Marshall Space Flight Center

1. Introduction

Both magnetic and gravitational fields play an important role in determining the evolution of the matter in many astrophysical objects. In highly conducting plasma, the magnetic field can be amplified by gas contraction or shear motion. Even when the magnetic field is weak initially, the magnetic field grows short time scales and influences the gas dynamics of the system. This is particularly important for a compact object such as a black hole or a neutron star. Relativistic jets have been observed or postulated in various astrophysical objects, including active galactic nuclei (AGNs) (e.g., Urry & Pavovani 1995; Ferrari 1998; Blandford 2002), microquasars in our galaxy (e.g., Mirabel & Rodríguez 1999), and gamma-ray bursts (GRBs) (e.g., Zhang & Mészáros 2004; Piran 2005; Mészáros 2006). The most promising mechanisms for producing the relativistic jets involve the magnetohydrodynamic centrifugal acceleration and/or magnetic pressure driven acceleration from the accretion disk with the compact objects (e.g., Blandford & Payne 1982; Fukue 1990), or the extraction of rotating energy from the rotating black hole (Penrose 1969; Blandford & Znajek 1977). In addition, the differential rotation of the plasma in the disk raises the magnetorotational instability (MRI), which plays an important role for the transportation of angular momentum from the disk due to the associated turbulence in accretion disks (Balbus & Hawley 1991, 1998). It is much more efficient than the internal disk transport. Magnetars are neutron stars with extremely large magnetic fields ($\sim 10^{14} - 10^{15}G$), as inferred from studies of anomalous X-ray pulsars and soft gamma-ray repeaters (e.g., Woods & Thompson 2006)). These intense magnetic fields are expected to affect the internal structure of the neutron star (e.g., Bocquet et al. 1995). The less intense fields of other neutron stars, $\sim 10^{12} - 10^{13}G$, may also affect the internal structure.

There has been much progress in the analytical studies of relativistic astrophysical phenomena (e.g., Camenzind 1990; Fendt 1997; Fendt & Ouyed 2004). However, the problem is complex, involving time-dependent, three-dimensional dynamics of magnetized plasmas in the relativistic potential. Therefore analytical solutions are rather limited to simplified cases that are time stationary and spatially symmetric. Because of these, numerical experiments play an important role for complementing theoretical works.

A complete review of numerical approaches to relativistic hydrodynamics is given by Martí & Müller (2003) and Font (2003). Numerical codes in special relativistic magnetohydrodynamics (SRMHD) have been developed by a growing number of authors (van Putten 1993; Koide et al. 1996; Komissarov 1999a; Balsara 2001; Koldoba et al. 2002; Del Zanna, Buccianti, & Londrillo 2003; Leismann et al. 2005; Mignone & Bodo 2006) and have been applied to the study of the relativistic jets (Koide et al. 1996, 1997; Koide 1997; Nishikawa et al. 1997, 1998; Komissarov 1999b; Leismann et al. 2005; Mignone & Bodo 2006) and

pulsar wind nebulae (Komissarov & Lyubarsky 2003, 2004; Bucciantini et al. 2003, 2004, 2005, 2006; Del Zanna et al. 2004). In addition, Komissarov (1999a) and Balsara (2001) proposed a comprehensive set of tests to validate numerical codes in special relativity. The exact solutions of the Riemann problem in the SRMHD have been obtained by Giacomazzo & Rezzolla (2006).

In order to investigate relativistic magnetorotators (RMRs), general relativistic magnetohydrodynamics (GRMHD) codes with fixed spacetimes have been developed by some authors (Yokosawa 1993; Koide et al. 1998; De Villiers & Hawley 2003; Gammie et al. 2003; Komissarov 2004; Antón et al. 2005; Anninos et al. 2005). These codes have been used to study the structure of accretion flows onto Kerr black holes and/or the formation of jets (Yokosawa 1995; Koide et al. 1998, 1999, 2000; Nishikawa et al. 2005; De Villiers et al. 2003, 2005a; Hirose et al. 2004; Krolik et al. 2005; Hawley & Krolik 2006; McKinney & Gammie 2004; McKinney 2005, 2006), the Blandford-Znajek effect near the rotating black hole (Koide et al. 2002; Koide 2003; Komissarov 2005), and the formation of GRB jets in collapsars (Mizuno et al. 2004a, 2004b; De Villiers et al. 2005b).

Few attempts have been made to simulate relativistic MHD flows in dynamical spacetimes (e.g., Wilson 1975, Baumgarte & Shapiro 2003). Recently new codes capable of evolving the Einstein-Maxwell-MHD equations have been developed by Duez et al. (2005), Shibata & Sekiguchi (2005) and Anderson et al. (2006). These codes have been applied to investigate rotating neutron stars (Duez et al. 2006a,b), and collapsing neutron stars for a central engine for short gamma-ray bursts (Shibata et al. 2006). These new GRMHD simulations with dynamical spacetimes will be applied to investigate various astrophysical systems such as merging neutron stars and black holes including gravitational waves and relativistic jets (e.g., Duez et al. 2005).

Our previous GRMHD code developed by Koide has been applied to many high-energy astrophysical phenomena and showed pioneering results (Koide et al. 1998, 1999, 2000, 2002; Koide 2003, 2004, 2006; Mizuno et al. 2004a,b; Nishikawa et al. 2005). However, the code cannot perform calculations in highly relativistic or highly magnetized regimes. The critical problem of the previous GRMHD code is that it cannot guarantee a divergence-free magnetic field. Even though we introduce a divergence-cleaning step in the code, it cannot perform long-term evolution, except in special cases. In order to overcome these numerical difficulties, we have developed a new, three-dimensional, GRMHD code called RAISHIN, for RelAtIviStic magnetoHydrodynamic sImulatioN. (RAISHIN is the ancient Japanese god of lightning.) It uses a conservative, high resolution shock-capturing scheme.

The structure of the paper is as follows. In section 2 we describe the basic equations of GRMHD including the essentials of the 3+1 formalism, the description of the magnetic

field, the induction equation and the conservation equations of particle number, and the stress-energy tensor in conservative form. In section 3 we describe the basic algorithm of our new GRMHD code based on the recent modern techniques such as HLL approximate Riemann solver, various reconstruction methods and flux-interpolated constrained transport. We show the performance of the code on a series of test problems in section 4. The summary and conclusions are given in section 5.

The new simulation results of jet formation using this code will be reported separately (Mizuno et al. 2006).

2. Basic Equations

2.1. Spacetimes and observers

We investigate the evolution of a magnetized fluid in the background spacetime metric of a black hole written as

$$ds^2 = -\alpha^2 dt^2 + \gamma_{ij}(dx^i + \beta^i dt)(dx^j + \beta^j dt), \quad (1)$$

where α , β^i , and γ_{ij} are the lapse function, shift vector, and spatial metric respectively. A natural observer associated in the metric given by Eq. (1) is the so-called Eulerian observer with four-velocity u^μ perpendicular to the hypersurfaces of constant t at each event in the spacetime. The covariant and contravariant components of n^μ are given by

$$n^\mu = \frac{1}{\alpha}(1, -\beta^i), \quad (2)$$

and

$$n_\mu = (-\alpha, 0, 0, 0), \quad (3)$$

respectively.

The comoving observer follows the fluid motion with four-velocity u^μ . The three-velocity of the fluid as measured by the Eulerian observer can be given as

$$v^i \equiv -\frac{h_j^i u^\mu}{n_\mu u^\mu}, \quad (4)$$

where $-n_\mu u^\mu \equiv W$ is the relative Lorentz factor between u^μ and n_μ and $h_{\mu\nu} = g_{\mu\nu} + n_\mu n_\nu$ is the projector tensor onto the hypersurface orthogonal to n^μ . The spatial component of the projector tensor is $h_{ij} = \gamma_{ij}$. Eq (4) is written as

$$v^i = \frac{u^i}{\alpha u^t} + \frac{\beta^i}{\alpha}, \quad (5)$$

and

$$v_i = u_i/\gamma. \quad (6)$$

The Lorentz factor satisfies the following relation

$$\gamma = \frac{1}{\sqrt{(1 - v^2)}} = \alpha u^t, \quad (7)$$

where $v^2 = \gamma_{ij}v^iv^j$.

2.2. Evolution of the electromagnetic fields

The electromagnetic field in general relativity is described by the Faraday electromagnetic tensor $F^{\mu\nu}$. This tensor is related to the electric field E^μ and magnetic field B^μ measured by the Eulerian observer,

$$F^{\mu\nu} = n^\mu E^\nu - n^\nu E^\mu + n_\gamma \epsilon^{\gamma\mu\nu\sigma} B_\sigma, \quad (8)$$

where $\epsilon^{\gamma\mu\nu\sigma} = (-g)^{1/2}[\gamma\mu\nu\sigma]$, g is the determinant of the four-metric ($g = \det g_{\mu\nu}$) and $\epsilon^{\gamma\mu\nu\sigma}$ is the antisymmetric Levi-Civita symbol. Both electric and magnetic fields are orthogonal to n^μ ($E^\mu n_\mu = B^\mu n_\mu = 0$), and can be expressed as

$$E^\mu = F^{\mu\nu} n_\nu, \quad (9)$$

and

$$B^\mu = \frac{1}{2} \epsilon^{\mu\nu\kappa\lambda} n_\nu F_{\kappa\lambda} = n_\nu F^{*\nu\mu}, \quad (10)$$

where

$$F^{*\mu\nu} = \frac{1}{2} \epsilon^{\mu\nu\kappa\lambda} F_{\kappa\lambda} \quad (11)$$

is dual of the electromagnetic field tensor.

We adopt the ideal MHD condition and assume that the fluid is a perfect conductor. In this case the fluid has infinite conductivity and in order to keep the current finite, the conduction current must vanish

$$F^{\mu\nu} u_\nu = 0 \quad (12)$$

which means that the electric field in the rest frame of the fluid is zero. The electric and magnetic fields measured by a comoving observer are

$$\hat{E}^\mu = F^{\mu\nu} u_\nu, \quad (13)$$

and

$$\hat{B}^\mu = u_\nu F^{*\nu\mu}. \quad (14)$$

The ideal MHD condition (12) satisfies the condition that the electric field observed by a comoving observer becomes zero ($\hat{E}^\mu = 0$). \hat{B}^μ is orthogonal to u_μ , i.e. $u_\mu \hat{B}^\mu = 0$. The electromagnetic tensor can be expressed by the terms of \hat{B}^μ as

$$F^{\mu\nu} = u_\gamma \epsilon^{\gamma\mu\nu\sigma} \hat{B}_\sigma. \quad (15)$$

The dual of the electromagnetic field tensor is also obtained by

$$F^{*\mu\nu} = \hat{B}^\mu u^\nu - \hat{B}^\nu u^\mu. \quad (16)$$

Since \hat{B}^μ is orthogonal to u_μ , we have $h_\nu^\mu \hat{B}^\nu = \hat{B}^\mu$. From Eqs. (10) and (16)

$$h_\nu^\mu B^\nu = -n_\lambda u^\lambda \hat{B}^\mu. \quad (17)$$

Therefore

$$\hat{B}^\mu = -\frac{h_\nu^\mu B^\nu}{n_\nu u^\nu}. \quad (18)$$

The time and space components of Eq. (18) are given by

$$\hat{B}^t = \frac{\gamma v_i B^i}{\alpha}, \quad (19)$$

and

$$\hat{B}^i = \frac{B^i + \alpha \hat{B}^t u^i}{\alpha u^t}. \quad (20)$$

The evolution equation for the magnetic field can be obtained in conservation form from the dual of Maxwell's equation

$$F_{\mu\nu,\lambda} + F_{\lambda\mu,\nu} + F_{\nu\lambda,\mu} = 0 \quad (21)$$

in a coordinate basis,

$$F_{;\nu}^{*\mu\nu} = \frac{1}{\sqrt{-g}} \frac{\partial}{\partial x^\nu} (\sqrt{-g} F^{*\mu\nu}) = 0. \quad (22)$$

Since $\sqrt{-g} = \alpha \sqrt{\gamma}$ and $F^{*it} = B^i/\alpha$, the time component of Eq. (22) gives the divergence-free magnetic field constraint

$$\frac{1}{\sqrt{-g}} \frac{\partial}{\partial x^i} (\sqrt{\gamma} B^i) = 0, \quad (23)$$

and the spatial components of Eq. (22) gives the induction equation

$$\frac{1}{\sqrt{-g}} \frac{\partial}{\partial t} (\sqrt{\gamma} B^i) + \frac{1}{\sqrt{-g}} \frac{\partial}{\partial x^i} [\sqrt{-g} (u^j \hat{B}^i - u^i \hat{B}^j)] = 0. \quad (24)$$

It follows from Eq. (20) that

$$u^j \hat{B}^i - u^i \hat{B}^j = (\tilde{v}^j B^i - \tilde{v}^i B^j), \quad (25)$$

where $\tilde{v}^i = v^i - \beta^i/\alpha$. Therefore the induction equation can be written as

$$\frac{1}{\sqrt{-g}} \frac{\partial}{\partial t} (\sqrt{\gamma} B^i) + \frac{1}{\sqrt{-g}} \frac{\partial}{\partial x^i} [\sqrt{-g} (\tilde{v}^j B^i - \tilde{v}^i B^j)] = 0. \quad (26)$$

2.3. Conservation Equations

The evolution equations for matter can be expressed as the local conservation laws for particle number and energy-momentum. The particle number conservation equation is written as

$$(\rho u^\mu)_{;\mu} = 0. \quad (27)$$

Here ρ is the rest-mass density. In a coordinate basis we rewrite this as

$$\frac{1}{\sqrt{-g}} \frac{\partial}{\partial x^\mu} (\sqrt{-g} \rho u^\mu) = 0, \quad (28)$$

and in 3+1 formalism

$$\frac{1}{\sqrt{-g}} \frac{\partial}{\partial t} (\sqrt{\gamma} D) + \frac{1}{\sqrt{-g}} \frac{\partial}{\partial x^i} (\sqrt{-g} D \tilde{v}^i) = 0, \quad (29)$$

where $D = \gamma \rho$.

The energy-momentum conservation equation is given by

$$T^{\mu\nu}_{;\nu} = 0, \quad (30)$$

where $T^{\mu\nu}$ is the energy-momentum tensor. In a coordinate basis we rewrite this as

$$\frac{1}{\sqrt{-g}} \frac{\partial}{\partial x^\nu} (\sqrt{-g} T^{\mu\nu}) = 0, \quad (31)$$

and in 3+1 formalism

$$\frac{1}{\sqrt{-g}} \frac{\partial}{\partial t} (\sqrt{-g} T^{t\nu}) + \frac{1}{\sqrt{-g}} \frac{\partial}{\partial x^i} (\sqrt{-g} T^{i\nu}) - \Gamma^\mu_{\sigma\nu} T^{\sigma\nu} = 0, \quad (32)$$

where $\Gamma^\mu_{\sigma\nu}$ is the Christoffel symbol. The energy-momentum tensor for a system containing a perfect fluid and an electromagnetic field is the sum of a fluid part,

$$T^{\mu\nu}_{\text{fluid}} = \rho h u^\mu u^\nu + p g^{\mu\nu}, \quad (33)$$

where p is pressure, h is the specific enthalpy, defined by $h = 1 + u + p/\rho$ and u is internal energy and an electromagnetic part,

$$T_{\text{EM}}^{\mu\nu} = \frac{1}{4\pi} \left(F^{\mu\lambda} F_{\lambda}^{\nu} - \frac{1}{4} g^{\mu\nu} F_{\alpha\beta} F^{\alpha\beta} \right). \quad (34)$$

In the ideal MHD condition, $T_{\text{EM}}^{\mu\nu}$ can be expressed simply in term of a magnetic 4-vector $b^\mu = \hat{B}^\mu/\sqrt{4\pi}$ as (e.g., Eq. (15))

$$T_{\text{EM}}^{\mu\nu} = b^2 u^\mu u^\nu + \frac{b^2}{2} g^{\mu\nu} - b^\mu b^\nu, \quad (35)$$

where $b^2 = b^\nu b_\nu$. Hence the energy-momentum tensor is given by

$$T^{\mu\nu} = (\rho h + b^2) u^\mu u^\nu + \left(p + \frac{b^2}{2} \right) g^{\mu\nu} - b^\mu b^\nu. \quad (36)$$

The spatial components of the energy-momentum conservation equation give the momentum equation

$$\frac{1}{\sqrt{-g}} \frac{\partial}{\partial t} (\sqrt{\gamma} S_i) + \frac{1}{\sqrt{-g}} \frac{\partial}{\partial x^i} (\sqrt{-g} T_i^j) = T^{\mu\nu} \left(\frac{\partial g_{\nu i}}{\partial x^\mu} - \Gamma_{\nu\mu}^\sigma g_{\sigma i} \right), \quad (37)$$

where S_i is the momentum density of the magnetized fluid

$$S_i = \alpha T_i^t = (\rho h + b^2) \gamma^2 v_j - \alpha b^t b_j. \quad (38)$$

The time component of the energy-momentum conservation equation gives the energy equation

$$\frac{1}{\sqrt{-g}} \frac{\partial}{\partial t} (\sqrt{\gamma} \tau) + \frac{1}{\sqrt{-g}} \frac{\partial}{\partial x^i} [\sqrt{-g} (\alpha T^{ti} - D \tilde{v}^i)] = \alpha \left(T^{\mu t} \frac{\partial \ln \alpha}{\partial x^\mu} - T^{\mu\nu} \Gamma_{\nu\mu}^t \right), \quad (39)$$

where τ is the total energy density

$$\tau = \alpha^2 T^{tt} - D = (\rho h + b^2) \gamma^2 - (p + b^2/2) - \alpha^2 (b^t)^2 - D. \quad (40)$$

To complete the system of equations, it remains to specify the equation of state (EOS). In this paper we adopt a Γ -law EOS

$$p = (\Gamma - 1) \rho u, \quad (41)$$

where Γ is adiabatic index.

In summary, the evolution equations of GRMHD can be written in the following general form

$$\frac{1}{\sqrt{-g}} \frac{\partial \sqrt{\gamma} \mathbf{U}}{\partial t} = - \frac{1}{\sqrt{-g}} \frac{\partial \sqrt{-g} \mathbf{F}}{\partial x^i} + \mathbf{S}, \quad (42)$$

where the quantities \mathbf{U} , \mathbf{F} , and \mathbf{S} are

$$\mathbf{U} = \begin{bmatrix} D \\ S_i \\ \tau \\ B^j \end{bmatrix}, \quad (43)$$

$$\mathbf{F} = \begin{bmatrix} D\tilde{v}^i \\ T_i^j \\ \alpha T^{ti} - D\tilde{v}^i \\ \tilde{v}^i B^j - \tilde{v}^j B^i \end{bmatrix}, \quad (44)$$

and

$$\mathbf{S} = \begin{bmatrix} 0 \\ T^{\mu\nu} \left(\frac{\partial g_{\nu i}}{\partial x^\mu} - \Gamma_{\nu\mu}^\sigma g_{\sigma i} \right) \\ \alpha \left(T^{\mu t} \frac{\partial \ln \alpha}{\partial x^\mu} - T^{\mu\nu} \Gamma_{\nu\mu}^t \right) \\ 0^j \end{bmatrix}, \quad (45)$$

where $0^j \equiv (0, 0, 0)^T$.

3. Numerical Scheme

Numerical evolution of the GRMHD equations involves determining the fundamental MHD variables $\mathbf{P} = (\rho, p, v^i, B^i)$, called the “primitive” variables, at future times, given initial values of \mathbf{P}_0 . The evolution equations of GRMHD are written in conserved form (e.g., Eqs. (42)-(45)). They give the time derivatives for “conserved” variables $\mathbf{U}(\mathbf{P}) = (D, S_i, \tau, B^i)$ in terms of source variables $\mathbf{S}(\mathbf{P})$ and the divergence of flux variables \mathbf{F} ;

$$\frac{\partial \mathbf{U}}{\partial t} = -\frac{\partial \mathbf{F}}{\partial x^i} + \mathbf{S} \equiv L(\mathbf{U}). \quad (46)$$

There are several ways to evolve the GRMHD equations numerically. Conservative schemes evolve \mathbf{U} with equation (46) at each time step. The advantage of these schemes is that highly accurate shock-capturing schemes can be applied to the GRMHD equations. The disadvantage is that these schemes must recover \mathbf{P} by numerically solving the system of equations, $\mathbf{U} = \mathbf{U}(\mathbf{P})$, after each time step. This can be complicated. Conservative schemes for GRMHD have been developed by Koide et al. (1999), Koide (2003), Gammie et al. (2003), Komissarov (2004), Duez et al.(2005), Shibata & Sekiguchi (2005) and Antón et al.(2006).

On the other hand non-conservative schemes such as ZEUS (Stone & Norman 1992) evolve variables which are more simple with respect to \mathbf{P} , but whose evolving equations are not the same form of Eq. (46). In such schemes, high resolution shock-capturing schemes cannot be applied and artificial viscosity must be used for handling discontinuities. The advantage of these schemes is they solve the internal energy equation instead of the energy equations (Eq. (39)). This is an advantage in regions where the internal energy is small compared to the total energy (such as highly supersonic flows). Moreover, the recovery of \mathbf{P} is fairly straightforward. Non-conservative schemes for GRMHD have been developed by De Villiers & Hawley (2003) and Anninos et al. (2005).

Our GRMHD code described in detail in the following section employs conservative schemes to solve the three-dimensional GRMHD equations on uniform and non-uniform grids in each spatial direction (method of lines). To maintain flexibility our GRMHD code is programmed to allow for different boundary conditions, different coordinates (Cartesian, Cylindrical and Spherical in RMHD and Boyer-Lindquist coordinates in both non-rotating and rotating black holes), different spatial reconstruction algorithms, different time advance algorithms, and different recovery schemes.

3.1. The reconstruction step

In order to improve the spatial accuracy of the code, we interpolate the primitive variables within computational zones. These reconstructed variables are used to compute the fluxes \mathbf{F} . For simplicity, we will consider the one-dimensional case. The generalization to three dimensions is straightforward. The primitive variables to the left and right of the grid cell interface are $\mathbf{P}_L = \mathbf{P}_{i+1/2-\epsilon}$ and $\mathbf{P}_R = \mathbf{P}_{i+1/2+\epsilon}$ respectively. We have implemented several reconstruction schemes for computing \mathbf{P}_L and \mathbf{P}_R .

1) Piecewise linear method (PLM) reconstruction

We use the minmod slope-limited linear interpolation method and Monotonized central (MC) slope-limited linear interpolation method (van Leer 1977). These methods give results with the second-order accuracy at smooth regions and switch to first-order at local extrema. For given primitive variables a , values of a at the left and right of the grid cell interface a_L and a_R are computed according to

$$a_L = a_i + \nabla a_i \Delta x / 2 \tag{47}$$

$$a_R = a_{i+1} - \nabla a_{i+1} \Delta x / 2 \tag{48}$$

Here, ∇a is the slope-limited gradient of a .

In the minmod slope limited linear interpolation method,

$$\nabla a = \Delta x^{-1} \text{minmod}(a_{i+1} - a_i, a_i - a_{i-1}), \quad (49)$$

$$\text{minmod}(a, b) = \begin{cases} 0 & \text{if } ab \leq 0, \\ \text{sign}(a) \min(|a|, |b|) & \text{otherwise.} \end{cases} \quad (50)$$

In the MC slope-limited linear interpolation method,

$$\nabla a = \Delta x^{-1} \text{MC}(a_{i+1} - a_i, a_i - a_{i-1}), \quad (51)$$

$$\text{MC}(a, b) = \begin{cases} 0 & \text{if } ab \leq 0, \\ \text{sign}(a) \min(2|a|, 2|b|, |a + b|/2) & \text{otherwise.} \end{cases} \quad (52)$$

2) Convex, essentially non-oscillatory (CENO) reconstruction

In this scheme, polynomial (quadratic) interpolation is used to obtain the primitive variables of the left and right of the grid cell interface. In smooth regions, these values are accurate to third order in Δx . The scheme becomes first order at local extrema. The details of this scheme are written in Del Zanna & Bucciantini (2002) and Del Zanna et al. (2003).

3) Piecewise parabolic method (PPM) reconstruction

In this scheme, the quadratic polynomial interpolation is used to obtain the primitive variables to the left and right of the grid cell interface. These reconstructed values are then modified such that the parabolic profile defined by a_L , a_R and a_i is monotonic inside the grid cell. The modified interpolated values at the grid cell interfaces define local Riemann problems. In the regions near the contact discontinuities, the interpolation procedure is modified slightly to account sharp jumps. In the vicinity of the local extrema, the scheme switches to a piecewise constant approximation in order to avoid post shock oscillations. In smooth regions, these values are accurate to fourth order in Δx . The scheme becomes first order at local extrema. The details of this scheme are written in Colella & Woodward (1984) and the relativistic version of the PPM algorithm is written in Martí and Müller (1996).

3.2. The Riemann solver step

To calculate the numerical flux, we use the HLL (Harten, Lax, and van Leer) approximate Riemann solver (Harten et al. 1983). The HLL approximate Riemann solver is one of the simplest shock-capturing schemes because it does not require the eigenvector of the

characteristic matrix. However, when it couples with a high-order reconstruction scheme, it has been shown to perform with an accuracy comparable to more sophisticated solvers in shock tube problems (Del Zanna & Buccianitni 2002; Lucas-Serrano et al. 2004). To calculate the HLL fluxes, one only needs to know a maximum left-going wave speed c_+ and a maximum right-going wave speed c_- at the both sides of the grid cell interface.

From \mathbf{P}_R and \mathbf{P}_L , we calculate the maximum left-going wave speeds $c_{\pm,L}$, the maximum right-going wave speeds $c_{\pm,R}$, the fluxes $\mathbf{F}_R = \mathbf{F}(\mathbf{P}_R)$ and $\mathbf{F}_L = \mathbf{F}(\mathbf{P}_L)$, and conserved variables $\mathbf{U}_R = \mathbf{U}(\mathbf{P}_R)$ and $\mathbf{U}_L = \mathbf{U}(\mathbf{P}_L)$. Defining $c_{\max} \equiv \max(0, c_{+,R}, c_{+,L})$ and $c_{\min} \equiv -\min(0, c_{-,R}, c_{-,L})$, the HLL flux is given by

$$\mathbf{F}_{i+1/2} = \frac{c_{\min}\mathbf{F}_R + c_{\max}\mathbf{F}_L - c_{\min}c_{\max}(\mathbf{U}_R - \mathbf{U}_L)}{c_{\max} + c_{\min}}. \quad (53)$$

We calculate the wave speeds c_{\pm} by the same method as Gammie et al. (2003) and Duez et al. (2005). The HLL approximate Riemann solver requires only the maximum wave speeds in either direction along the three coordinate axes. To determine the wave speeds in the x^1 direction, one solves the dispersion relation for MHD waves with wave vectors of the form

$$k_{\mu} = (-\omega, k_1, 0, 0). \quad (54)$$

The wave speed is the phase speed ω/k_1 . The speeds along the x^2 and x^3 direction are calculated in a similar way. The full dispersion relation for fast and slow modes is a fourth-order polynomial. It is difficult to solve the full dispersion relation. Gammie et al. (2003) has proposed replacing the full dispersion relation by the simpler approximate expression which overestimates the maximum speeds by a factor of ≤ 2 (it makes the evolution more diffusive but more stable). In the frame comoving with the fluid, the approximate dispersion relation for slow and fast modes is written by

$$\omega^2 = [v_A^2 + c_s^2(1 - v_A^2)]k^2, \quad (55)$$

where $c_s = \sqrt{\Gamma p/(\rho h)}$ is the sound speed, v_A is the Alfvén speed, $v_A^2 = b^2/(\rho h + b^2)$.

3.3. Constrained transport

High resolution shock-capturing scheme can successfully solve many problems involving various kinds of discontinuities. However these schemes do not guarantee $\nabla \cdot \mathbf{B} = 0$ in multidimensional simulations. Therefore we need to use constrained transport schemes to evolve the induction equation while maintaining $\nabla \cdot \mathbf{B} = 0$.

Several approaches and schemes have been proposed to maintain $\nabla \cdot \mathbf{B} = 0$ (e.g., Tóth 2002). We use the flux-interpolated, constrained transport (flux-CT) scheme introduced by Tóth (2002) and used by Gammie et al. (2003) and Duez et al. (2005). This scheme involves replacing the numerical flux of the induction equation computed at each point with linear combinations of the numerical fluxes computed at that point and neighboring points. The merit of this scheme is that it is naturally coupled with a Godunov-type scheme (Tóth 2002; Gammie et al 2003). It does not need the staggered variables which are needed in the constrained transport scheme by Evans & Hawley (1988), and the advantage of its usage with higher order implementation of the divergence free condition is discussed in Londrillo & Del Zanna (2004).

3.4. Time advance step

In the time advance step, we get the updated values of the conserved variables at the next time levels (\mathbf{U}^{n+1}). We use a multistep TVD Runge-Kutta (RK) method developed by Shu & Osher (1988) that can provide second (RK2) and third (RK3) order accuracy in time. The explicit form of the algorithms is:

1. Prediction step (common for RK2 and RK3):

$$\mathbf{U}^{(1)} = \mathbf{U}^n + \Delta t L(\mathbf{U}^n). \quad (56)$$

2. Depending on the accuracy of the time advance scheme do:

RK2:

$$\mathbf{U}^{n+1} = \frac{1}{a}[b\mathbf{U}^n + \mathbf{U}^{(1)} + \Delta t L(\mathbf{U}^{(1)})], \quad (57)$$

in this case $a = 2$ and $b = 1$.

RK3:

$$\mathbf{U}^{(2)} = \frac{1}{a}[b\mathbf{U}^n + \mathbf{U}^{(1)} + \Delta t L(\mathbf{U}^{(1)})], \quad (58)$$

$$\mathbf{U}^{n+1} = \frac{1}{b}[\mathbf{U}^n + 2\mathbf{U}^{(2)} + 2\Delta t L(\mathbf{U}^{(2)})], \quad (59)$$

in this case $a = 4$ and $b = 3$.

3.5. Recovery of primitive variables

The conservative MHD scheme for GRMHD requires a method for transforming between conserved variables \mathbf{U} and primitive variables \mathbf{P} . The forward transformation (from primitive to conserved variables) has a closed-form solution, but the inverse transformation (from conserved to primitive variables) requires the solution of a set of five nonlinear equations. Having computed \mathbf{U} at the new timestep, we must calculate primitive variables \mathbf{P} at the new time.

For the recovery we prepare two methods, Koide’s 2D method (Koide et al. 1999) and Noble’s 2D method (Noble et al. 2006).

1. Koide’s 2D method

In Koide et al. (1999) they solve two nonlinear, simultaneous algebraic equations with two independent variables $x \equiv \gamma - 1$ and $y \equiv \gamma(\mathbf{v} \cdot \mathbf{B})$. In these equations they use Γ -law EOS (see Eq. (41))

$$\begin{aligned} x(x+2) \left[\Gamma R x^2 + (2\Gamma R - d)x + \Gamma R - d + e + \frac{\Gamma}{2} y^2 \right]^2 \\ = (\Gamma x^2 + 2\Gamma x + 1)^2 [f^2(x+1)^2 + 2\sigma y + 2\sigma xy + g^2 y^2], \end{aligned} \quad (60)$$

$$\begin{aligned} \left[\Gamma(R - g^2)x^2 + (2\Gamma R - 2\Gamma g^2 - d)x + \Gamma R - d + e - g^2 + \frac{\Gamma}{2} y^2 \right] y \\ = \sigma(x+1)(\Gamma x^2 + 2\Gamma x + 1), \end{aligned} \quad (61)$$

where $R = D + \tau$, $d = (\Gamma - 1)D$, $e = (1 - \Gamma/2)B^2$, $f = \mathbf{S}$, $g = \mathbf{B}$, and $\sigma = \mathbf{B} \cdot \mathbf{S}$. Note that, in the absence of the magnetic field B^i , Eq (60) reduces to the well-known relativistic hydrodynamic one derived by Duncan and Hughes (1994), and Eq (61) becomes a trivial equation. These algebraic equations are solved at each grid cell using a 2-variable Newton-Raphson iteration method. The primitive variables then are calculated easily from x , y , D , \mathbf{S} , τ , and \mathbf{B} , using

$$\gamma = 1 + x, \quad (62)$$

$$p = \frac{(\Gamma - 1)[\tau - xD - (2 - 1/\gamma^2)B^2/2 + (y/\gamma)^2/2]}{[\gamma x(x+2) + 1]}, \quad (63)$$

and

$$\mathbf{v} = \frac{\mathbf{S} + (y/\gamma)\mathbf{B}}{D + \{\tau + p + B^2/2\gamma^2 + (y/\gamma)^2/2\}}. \quad (64)$$

This method is identical to that used in special relativistic MHD simulations (Koide, Nishikawa, & Mutel 1996; Koide 1997).

2. Noble’s 2D method

In Noble et al. (2006) they have tried six numerical methods for performing the inverse transformation and discuss the mathematical properties of them. We use one method which is recommended in Noble et al. (2006). This method solves two simple algebraic equations simultaneously for two independent variables $W \equiv \gamma^2 h$ and v^2

$$S^2 = (W + B^2)v^2 - \frac{(B^2 + 2W)(\mathbf{S} \cdot \mathbf{B})^2}{W^2}, \quad (65)$$

and

$$\tau = \frac{B^2}{2}(1 + v^2) + \frac{\mathbf{S} \cdot \mathbf{B}}{2W} + W - D - p(u, \rho). \quad (66)$$

and

Note that in Eq. (66) we can use any EOS. If we adopt a Γ -law EOS (Eq. (41)), Eq. (66) can be written as

$$\tau = \frac{B^2}{2}(1 + v^2) + \frac{\mathbf{S} \cdot \mathbf{B}}{2W} + W - D - \left(\frac{\Gamma - 1}{\Gamma} [(1 - v^2)W - \rho] \right). \quad (67)$$

These algebraic equations are solved at each grid cell using a 2-variable Newton-Raphson iteration method. From W and v^2 the primitive variables ρ and p (or u) are calculated easily.

4. Code Tests

In this section, we test the capabilities of our new GRMHD code. The tests are non-relativistic, special relativistic and general relativistic.

4.1. Linear Alfvén wave propagation

The first test considers the propagation of a small-amplitude Alfvén wave in one dimension of Cartesian coordinates. The initial conditions are $\rho = 1.0$, $p = 1.0$, $v^x = 0.0$, $v^y = A \cos(kx)$, $v^z = 0.0$, $B^x = B_0$, $B^y = -B_0(A/v_A) \cos(kx)$, and $B^z = 0.0$, where $k = 2\pi$ and A is the amplitude. We use the parameters $B_0 = 1.0$ and $A = 0.01$. The fluid satisfies a Γ -law EOS with $\Gamma = 4/3$. The computational domain is $0 \leq x \leq 1.0$ and the boundary condition is periodic.

The simulation runs for a single wave period $2\pi/\omega$ ($t_{end} = 2\pi/\omega$), so that a perfect scheme would return to its initial state. We measure the L_1 norm of the difference between

the final state and the initial state for each primitive variables Q such as

$$L_1(\delta Q) = \int_{i=1}^N |Q(t = 0) - Q(t = t_{end})| dx \quad (68)$$

as a function of the computational zone number N .

Figure 1 shows the L_1 norm of the error in v^y ($Q = v^y$ in Eq (68)) for runs using the MC slope limiter, minmod slope limiter, CENO, and PPM reconstructions as the computational zone number N is increased. Courant number is 0.5 in all simulations. All reconstruction schemes show that the global order of convergence of the code is second order in small computational zone number N and tend to flatter than second order convergence. Even we use the higher order reconstruction schemes such as CENO or PPM reconstructions, the global order of convergence of the code is second order. It is because we use the flux-CT scheme to maintain divergence-free magnetic field. It has second-order accuracy. Even all reconstruction schemes show the second order convergence, MC slope-limiter and PPM reconstructions are more accurate than minmod slope limiter and CENO reconstruction schemes.

4.2. Relativistic MHD shock-tube tests

Shock-tube tests are the most basic test problems for MHD (HD) codes. Large sets of test-problems in relativistic MHD have been performed over the years (i.e., Komissarov 1999a; Balsara 2001). In some test problems the exact solution of the Riemann problem in relativistic MHD has been calculated by Giacomazzo & Rezzolla (2006).

We perform eight simulations of $B^x \neq 0$ cases which exact solutions obtained by Giacomazzo & Rezzolla (2006). Therefore we can compare the simulation results with the exact solutions directly. All tests start with discontinuous initial data at $x = 0$ (see Table 1) and with homogenous profiles on either side in Cartesian coordinates. We simulate from $t = 0$ to $t = t_{\text{final}}$ with different reconstruction schemes, where t_{final} is specified in Table 1 for each case. The fluid satisfies a Γ -law EOS. In all cases we use 400 computational zones with a Courant factor of 0.5.

The results of the simulations are shown in Fig 2 -17. All results show good agreement with the exact solutions. However, some small discontinuities and large shocks cannot be resolved exactly. This means that we need more computational zones to resolve all small discontinuities and large shocks exactly. Generally, the minmod slope limiter and CENO reconstructions are more diffusive than the MC slope limiter and PPM reconstructions because of the properties of the minmod function. On the other hand, although the MC slope limiter

and PPM reconstructions can resolve sharp discontinuities well, some small oscillations are seen at the discontinuities. The PPM reconstruction is the most accurate scheme to detect the discontinuities.

Our previous GRMHD code of Koide (2003) could not handle some extreme cases of relativistic MHD shock-tube tests shown in Table 1 such as Kommissarov: Shock-Tube test1, Balsara Test2 and Balsara Test3 for large discontinuities of the pressure and magnetic field, Kommissarov: Collision Test and Balsara Test3 for the highly relativistic flow even using different recovery methods such as Noble 2D method. However the new GRMHD code successfully handles the relativistic MHD shock-tube tests in Table 1. Therefore the new GRMHD code has substantial improvements over our previous GRMHD code (e.g., Koide 2003) and can operate in a regime with large discontinuities of physical quantities (4 order difference of pressure in Kommissarov: Collision Test and Balsara Test3), strong magnetic field ($\beta < 0.004$ and $\sigma > 570$ in Balsara Test 3, where $\beta = p_{gas}/p_{mag}$, $p_{mag} = b^2/2$, and $\sigma = |b^2|/\rho$) and highly relativistic flow ($\gamma > 22$ in Balsara Test 4). The limitation to handle the regimes of high Lorentz factor and of highly magnetized depends on the schemes to solve the GRMHD equations.

4.3. Magnetized Bondi flow

Next we check the code to verify it numerically maintains the time-dependent system of equations describing the stationary, spherically symmetric accretion of a perfect fluid onto a Schwarzschild black hole in the presence of a radial magnetic field. Spherically symmetric accretion (Bondi flow) onto the fixed background of the Schwarzschild black hole has an analytic solution (e.g., Shapiro & Teukolsky 1983) that can be compared with the results of our code. This test has been used by several authors (De Villiers & Hawley 2003; Gammie et al. 2003; Duez et al. 2005; Shibata & Sekiguchi 2005; Antón et al. 2006) in the validation of their GRMHD codes.

The initial setup consists of a perfect fluid which satisfies a Γ -law EOS with $\Gamma = 4/3$. The analytic solution is calculated in a manner similar to Koide et al. (1999) with constant parameter $H = \rho_0 h_0 = 1.3$ and $\rho_0 = 1.0$. The critical point of free-falling flow is located at $r_S = 3.0$. The radial magnetic field component is chosen to satisfy the divergence-free condition. Its strength is determined by the parameter B_0 at the critical radius of the flow. These initial conditions are evolved in time in a uniform radial grid covering the region $1.1r_S \leq r \leq 20r_S$.

Figure 18 shows the L_1 norm of the radial velocity v^x ($Q = v^x$ in Eq. (68)) of the

difference between the exact solution and the final state ($t_{end} = 50\tau_s$, $\tau_s = r_S/c$) in the $B_0 = 0.001\sqrt{\rho_0 c^2}$ case. The calculation of L_1 norm is taken in the region $1.5r_S \leq r \leq 18r_S$ to exclude boundary effects. The MC slope limiter and minmod slope limiter reconstructions show that the global order of convergence of the code is second order. The MC slope limiter reconstruction is more accurate than the minmod slope limiter reconstruction.

5. Summary and Conclusions

We have developed a new three-dimensional GRMHD code, RAISHIN, by using a conservative high resolution shock-capturing scheme. The numerical fluxes are calculated using the HLL approximate Riemann solver scheme. The flux-interpolated, constrained transport scheme is used to maintain a divergence-free magnetic field. Several reconstruction and time advance schemes can be chosen for the numerical accuracy and computational resources.

We have described several test problems in both special and general relativity. They have shown significant improvements over our previous GRMHD code (Koide 2003). Our new GRMHD code can perform in the regimes of high Lorentz factor ($\gamma > 20$) and high magnetic field ($\sigma > 550$), and in the presence of large discontinuity of density, pressure and magnetic field. We have compared the results of several reconstruction schemes. The code is second-order accurate even when we use the higher order reconstruction schemes such as CENO and PPM. Nevertheless, higher-order reconstruction schemes can provide more accurate results for some applications. The PPM reconstruction scheme allows the well-resolved detection of sharp discontinuities. We found the limitation to handle the regimes of high Lorentz factor and of highly magnetized depends on the schemes to solve the GRMHD equations.

We have performed several simulations of non-rotating and rotating black hole systems with a thin accretion disk (Mizuno et al. 2006). The simulation results show the formation of jets driven by the Lorentz force and the gas pressure. It appears that the rotating black hole creates an additional, faster, and more collimated inner outflow beside an outflow generated by the rotating accretion disk in the non-rotating black hole. Thus, kinematic jet structure could be a sensitive function of the black hole rotation.

Our new GRMHD code has proven to be accurate in second order and has successfully passed all applied tests including highly relativistic cases, and highly magnetized cases in both special and general relativity. We plan to apply this code to a number of high-energy astrophysical phenomena involving highly relativistic flows or compact objects with strong gravitational fields and magnetic fields.

Y. M. is a NASA Postdoctoral Program fellow at NASA Marshall Space Flight Center. He thanks the help of B. Giacomazzo for providing their calculation code to get exact the solution of RMHD Riemann problems. He also thanks G. Richardson, D. Hartmann, C. Fendt, and M. Camenzind for useful discussions. K. N. is partially supported by the National Science Foundation awards ATM-0100997, INT-9981508, and AST-0506719, and the National Aeronautic and Space Administration award NASA-INTEG04-0000-0046 to the Univ of Alabama in Huntsville. P.H. acknowledges partial support by a National Space Science and Technology (NSSTC/NASA) cooperative agreement NCC8-256 and NSF awards AST-0506666. The simulations have been performed on IBM p690 at the National Center for Supercomputing Applications (NCSA) which is supported by the NSF and Altix3700 BX2 at YITP in Kyoto University.

REFERENCES

- Anderson, M., Hirschmann, E., Liebling, A. L., & Neilsen, D. 2006, in preparation (gr-qc/0605102)
- Anninos, P., Fragile, P. C., & Salmonson, J. D. 2005, *ApJ*, 635, 723
- Antón, L., et al. 2006, *ApJ*, 637, 296
- Balbus, S. A. & Hawley, J. F. 1991, *ApJ*, 376, 214
- Balbus, S. A. & Hawley, J. F. 1998, *Rev. Mod. Phys.*, 70, 1
- Balsara, D. 2001, *ApJS*, 132, 83
- Baumgarte, T.W., & Shapiro, S. L. 2003, *ApJ*, 585, 921
- Blandford, R. D. & Znajek, R. L. 1977, *MNRAS*, 179, 433
- Blandford, R. D. & Payne, D. G. 1982, *MNRAS*, 199, 883
- Blandford, R. D. 2002, in *Lighthouses of the Universe: Most Luminous Celestial Objects and Their Use for Cosmology* ed. M. Gifanov, R. Sunyaev, & E. Churazov (Springer-Verlag), 381
- Bocquet, M., Bonazzola, S., Gourgoulhon, E., & Novak, J. 1995, *A&A*, 301, 757
- Bucciantini, N., Blondin, J. M., Del Zanna, L., & Amato, E. 2003, *A&A*, 405, 617

- Bucciantini, N., Bandiera, R., Blondin, J. M., Amato, E., & Del Zanna, L. 2004, *A&A*, 422, 609
- Bucciantini, N., Amato, E., & Del Zanna, L. 2005, *A&A*, 434, 189
- Bucciantini, N., Thompson, T. A., Arons, J., Quataert, E., & Del Zanna, L. 2006, *MNRAS*, 368, 1717
- Camenzind, M., 1990, Magnetized disk-winds and the origin of bipolar outflows, in: Klare, G. (Ed) *Rev. Mod. Astron.*, 3, Springer, Heidelberg, p. 234
- Colella, P. & Woodward, P. R. 1984, *J. Comput. Phys.*, 54, 174
- Del Zanna, L. & Bucciantini, N. 2002, *A&A*, 390, 1177
- Del Zanna, L., Bucciantini, N., & Londrillo, P. 2003, *A&A*, 400, 397
- Del Zanna, L., Amato, E., & Bucciantini, N. 2004, *A&A*, 421, 1063
- De Villiers, J.-P. & Hawley, J. F. 2003, *ApJ*, 589, 458
- De Villiers, J.-P., Hawley, J. F., & Krolik, J. H. 2003, *ApJ*, 599, 1238
- De Villiers, J.-P., Hawley, J. F., Krolik, J. H., & Hirose, S. 2005a, *ApJ*, 620, 878
- De Villiers, J.-P., Staff, J., & Ouyed, R. 2005b, in preparation (astro-ph/0502225)
- Duez, M. D., Liu, Y. T., Shapiro, S. L., & Stephens, B. C. 2005, *Phys. Rev. D*, 72, 024028
- Duez, M. D., Liu, Y. T., Shapiro, S. L., Shibata, M., & Stephens, B. C. 2006, *Phys. Rev. D*, 73, 104015
- Duez, M. D., Liu, Y. T., Shapiro, S. L., Shibata, M., & Stephens, B. C. 2006, *Phys. Rev. Lett.*, 96, 031101
- Duncan, G. C. & Hughes, P. A. 1994, *ApJ*, 436, L119
- Evans, C. R. & Hawley, J. F. 1988, *ApJ*, 332, 659
- Fendt, C. 1997, *A&A*, 319, 1025
- Fendt, C. & Ouyed, R. 2004, *ApJ*, 608, 378
- Ferrari, A. 1998, *ARA&A*, 36, 539
- Font, J. A. 2003, *Living Reviews in Relativity*, 6, 4

- Fukue, J. 1990, PASJ, 42, 793
- Gammie, C. F., McKinney, J. C., & Tóth, G. 2003, ApJ, 589, 444
- Giacomazzo, B. & Rezzolla, L. 2006, J. Fluid Mech., 562, 223
- Harten, A., Lax, P. D., & van Leer, B. J. 1983, SIAM Rev., 25, 35
- Hawley, J. F. & Krolik, J. H. 2006, ApJ, 641, 103
- Hirose, S., Krolik, J. H., De Villiers, J.-P., & Hawley, J. F. 2004, ApJ, 606, 1083
- Koide, S., Nishikawa, K.-I., & Mutel, R. L. 1996, ApJ, 463, L71
- Koide, S., Sakai, J.-I., Nishikawa, K.-I., & Mutel, R. L. 1996, ApJ, 464, 724
- Koide, S. 1997, ApJ, 478, 66
- Koide, S., Shibata, K., & Kudoh, T. 1998, ApJ, 495, L63
- . 1999, ApJ, 522, 727
- Koide, S., Meier, D. L., Shibata, K., & Kudoh, T. 2000, ApJ, 536, 668
- Koide, S., Shibata, K., Kudoh, T., & Meier, D. L. 2002, science, 295, 1688
- Koide, S. 2003, Phys. Rev. D, 67, 104010
- Koide, S. 2004, ApJ, 606, L45
- Koide, S., Kudoh, T., & Shibata, K. 2006, Phys. Rev. D, 74, 044005
- Koldoba, A. V., Kuznetsov, O. A., & Ustyugoya, G. V. 2002, MNRAS, 333, 932
- Komissarov, S. S. 1999a, MNRAS, 303, 343
- . 1999b, MNRAS, 308, 1069
- . 2004, MNRAS, 350, 1431
- . 2005, MNRAS, 359, 801
- Komissarov, S. S. & Lyubarsky, Y. E. 2003, MNRAS, 344, L93
- . 2004, MNRAS, 349, 779
- Krolik, J. H., Hawley, J. F., & Hirose, S. 2005, ApJ, 622, 1008

- Leismann, T., Antón, L., Aloy, M. A., Müller, E., Martí, J. M., Miralles, J. A., & Ibáñez, J. M. 2005, *A&A*, 436, 503
- Londrillo, P., & Del Zanna, L. 2004, *J. Comp. Phys.*, 195, 17
- Lucas-Serrano, A., Font, J. A., Ibáñez, J. M., & Martí, J. M. 2004, *A&A*, 428, 703
- Martí, J. M. & Müller, E. 1996, *J. Comput. Phys.*, 123, 1
- . 2003, *Living Reviews in Relativity*, 6, 7
- McKinney, J. C. 2005, *ApJ*, 630, L5
- . 2006, *MNRAS*, 368, 1561
- McKinney, J. C. & Gammie, C. F. 2004, *ApJ*, 977
- Mészáros, P. 2006, *Rep. Prog. Phys.*, in press (astro-ph/0605208)
- Mignone, A. & Bodo, G. 2006, *MNRAS*, 368, 1040
- Mirabel, I. F. & Rodríguez, L. F. 1999, *ARA&A*, 37, 409
- Mizuno, Y., Yamada, S., Koide, S., & Shibata, K. 2004a, *ApJ*, 606, 395
- . 2004b, *ApJ*, 615, 389
- Mizuno, Y., Nishikawa, K.-I., Koide, S., Hardee, P., & Fishman, G. J. 2006, *ApJ*, in preparaion
- Nishikawa, K.-I., Koide, S., Sakai, J.-I., Christodoulou, D. M., Sol, H., & Mutel, R. L. 1997, *ApJ*, 483, L45
- . 1998, *ApJ*, 498, 166
- Nishikawa, K.-I., Richardson, G., Koide, S., Shibata, K., Kudoh, T., Hardee, P., & Fishman, G. J. 2005, *ApJ*, 625, 60
- Noble, S. C., Gammie, C. F., McKinney, J. C., & Del Zanna, L. 2006, *ApJ*, 641, 626
- Penrose, R. 1969, *Nuovo Cimento*, 1, 252
- Piran, T. 2005, *Reviews of Modern Physics*, 76, 1143 (astro-ph/0405503)
- Shapiro, S. L., & Teukolsky, S. A. 1983, *Black Hole, White Dwarfs, and Neutron Stars: The Physics of Compact Objects* (New York: Wiley)

- Shibata, M. & Sekiguchi, Y.-I. 2005, *Phys. Rev. D*, 72, 044014
- Shibata, M., Duez, M. D., Liu, Y. T., Shapiro, S. L., & Stephens, B. C. 2006, *Phys. Rev. Lett.*, 96, 031102
- Shu, C. W. & Osher, S. J. 1988, *J. Comput. Phys.*, 77, 439
- Stone, J. M. & Norman, M. 1992, *ApJS*, 80, 791
- Tóth, G. 2000, *J. Comput. Phys.*, 161, 605
- Urry, C. M. & Padovani, P. 1995, *PASP*, 107, 803
- van Leer, B. J. 1977, *J. Comput. Phys.*, 23, 276
- van Putten, M. H. P. M., 1993, *ApJ*, 408, L21
- Wilson, J. R. 1975, *Ann. N.Y. Acad. Sci.* 262, 123
- Woods, P. M. & Thompson, C. 2006, in *Compact Stellar X-ray Sources* ed. W. H. G. Lewin & M. van der Klis (Cambridge: Cambridge Univ. Press), in press (astro-ph/0406133)
- Yokosawa, M. 1993, *PASJ*, 45, 218
- Yokosawa, M. 1995, *PASJ*, 47, 605
- Zhang, B. & Mészáros, P. 2004, *Int. J. Mod. Phys.*, A19, 2385 (astro-ph/0311321)

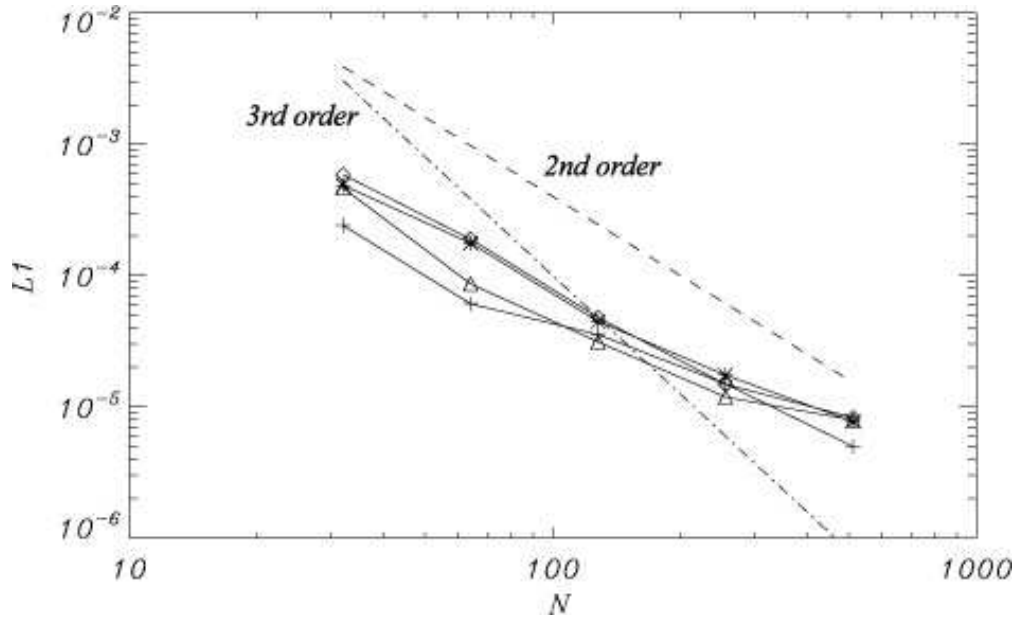


Fig. 1.— L_1 norm of the error in v^y for a linear Alfvén wave propagation as a function of computational zone number, N , for the MC slope limiter (plus), the minmod slope limiter (asterisk), convex CENO (open diamond) and PPM reconstructions (open triangle). The straight lines show the slope expected for second-order convergence (dashed line) and third-order convergence (dash-dotted line).

Table 1. Relativistic MHD Shock-Tube Tests

Test Type		ρ	p	v^x	v^y	v^z	B^x	B^y	B^z
Komissarov: Shock Tube Test1 $\Gamma = 4/3, t_{\text{final}} = 1.0$	<i>left state</i>	1.0	1000.0	0.0	0.0	0.0	1.0	0.0	0.0
	<i>right state</i>	0.1	1.0	0.0	0.0	0.0	1.0	0.0	0.0
Komissarov: Collision Test $\Gamma = 4/3, t_{\text{final}} = 1.2$	<i>left state</i>	1.0	1.0	$5/\sqrt{26}$	0.0	0.0	10.0	10.0	0.0
	<i>right state</i>	1.0	1.0	$-5/\sqrt{26}$	0.0	0.0	10.0	-10.0	0.0
Barsara Test1 (Brio & Wo) $\Gamma = 2, t_{\text{final}} = 0.4$	<i>left state</i>	1.000	1.0	0.0	0.0	0.0	0.5	1.0	0.0
	<i>right state</i>	0.125	0.1	0.0	0.0	0.0	0.5	-1.0	0.0
Barsara Test2 $\Gamma = 5/3, t_{\text{final}} = 0.4$	<i>left state</i>	1.0	30.0	0.0	0.0	0.0	5.0	6.0	6.0
	<i>right state</i>	1.0	1.0	0.0	0.0	0.0	5.0	0.7	0.7
Barsara Test3 $\Gamma = 5/3, t_{\text{final}} = 0.4$	<i>left state</i>	1.0	1000.0	0.0	0.0	0.0	10.0	7.0	7.0
	<i>right state</i>	1.0	0.1	0.0	0.0	0.0	10.0	0.7	0.7
Barsara Test4 $\Gamma = 5/3, t_{\text{final}} = 0.4$	<i>left state</i>	1.0	0.1	0.999	0.0	0.0	10.0	7.0	7.0
	<i>right state</i>	1.0	0.1	-0.999	0.0	0.0	10.0	-7.0	-7.0
Barsara Test5 $\Gamma = 5/3, t_{\text{final}} = 0.5$	<i>left state</i>	1.08	0.95	0.40	0.3	0.2	2.0	0.3	0.3
	<i>right state</i>	1.00	1.0	-0.45	-0.2	0.2	2.0	-0.7	0.5
Generic Alfvén Test $\Gamma = 5/3, t_{\text{final}} = 1.5$	<i>left state</i>	1.0	5.0	0.0	0.3	0.4	1.0	6.0	2.0
	<i>right state</i>	0.9	5.3	0.0	0.0	0.0	1.0	5.0	2.0

Note. — Initial conditions for the relativistic shock-tube tests.

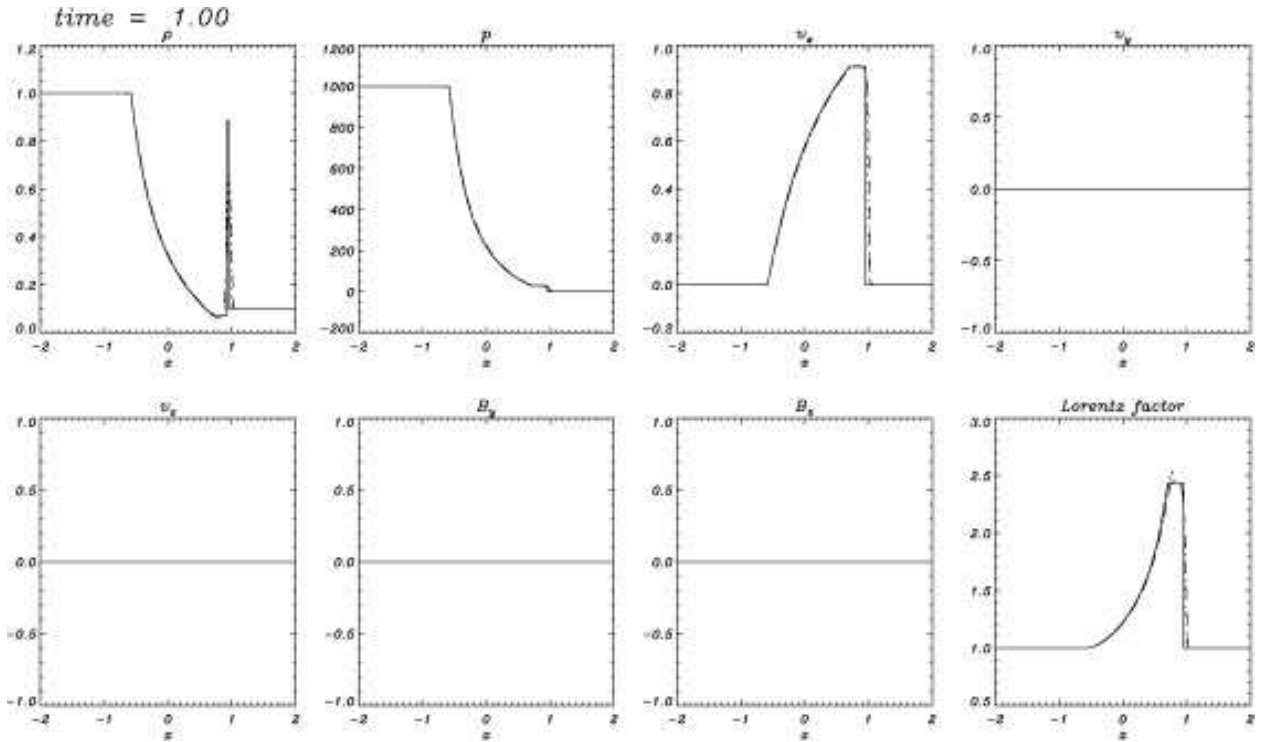


Fig. 2.— Simulation results of Komissarov shock-tube test 1 at time $t = 1.0$ using the MC slope limiter (dotted lines) and the minmod slope limiter (dashed lines) reconstructions. The solid lines are the exact solution. The results are composed of a left-going fast rarefaction, a contact discontinuity, and a right-going fast shock.

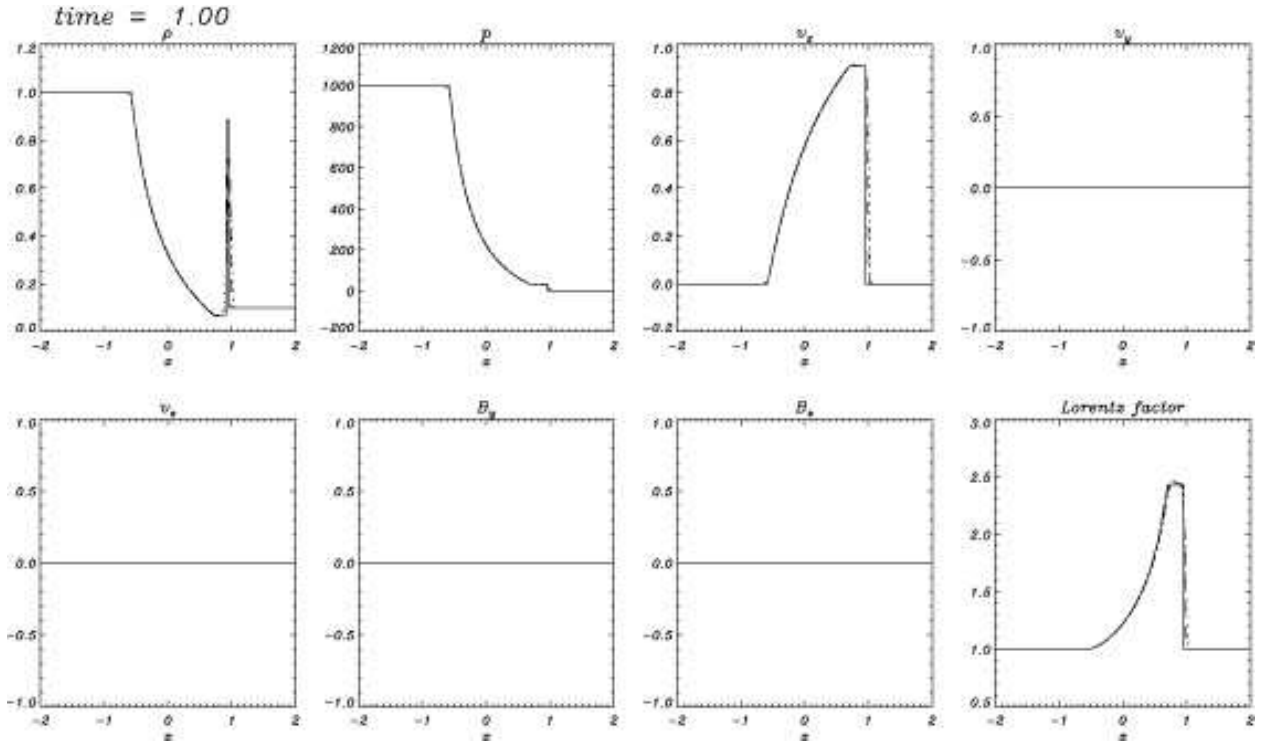


Fig. 3.— Simulation results of Komissarov shock-tube test 1 at time $t = 1.0$ using the CENO (dotted lines) and the PPM (dashed lines) reconstructions. The solid lines are the exact solution. The results are composed of a left-going fast rarefaction, a contact discontinuity, and a right-going fast shock.

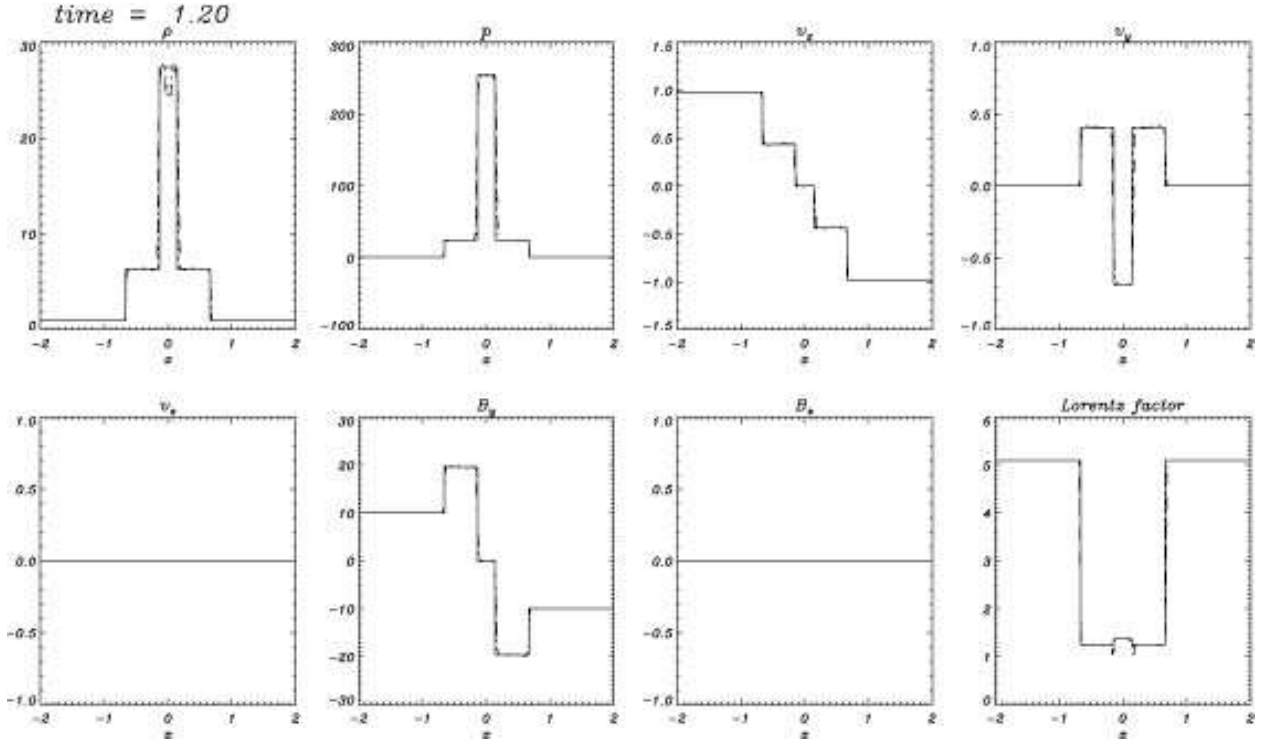


Fig. 4.— Simulation results of Komissarov collision test at time $t = 1.5$ using the MC slope limiter (dotted lines) and the minmod slope limiter (dashed lines) reconstructions. The solid lines are the exact solution. The results are composed of a left-going fast shock, of a left-going slow shock, a right-going slow shock, and a right-going fast shock.

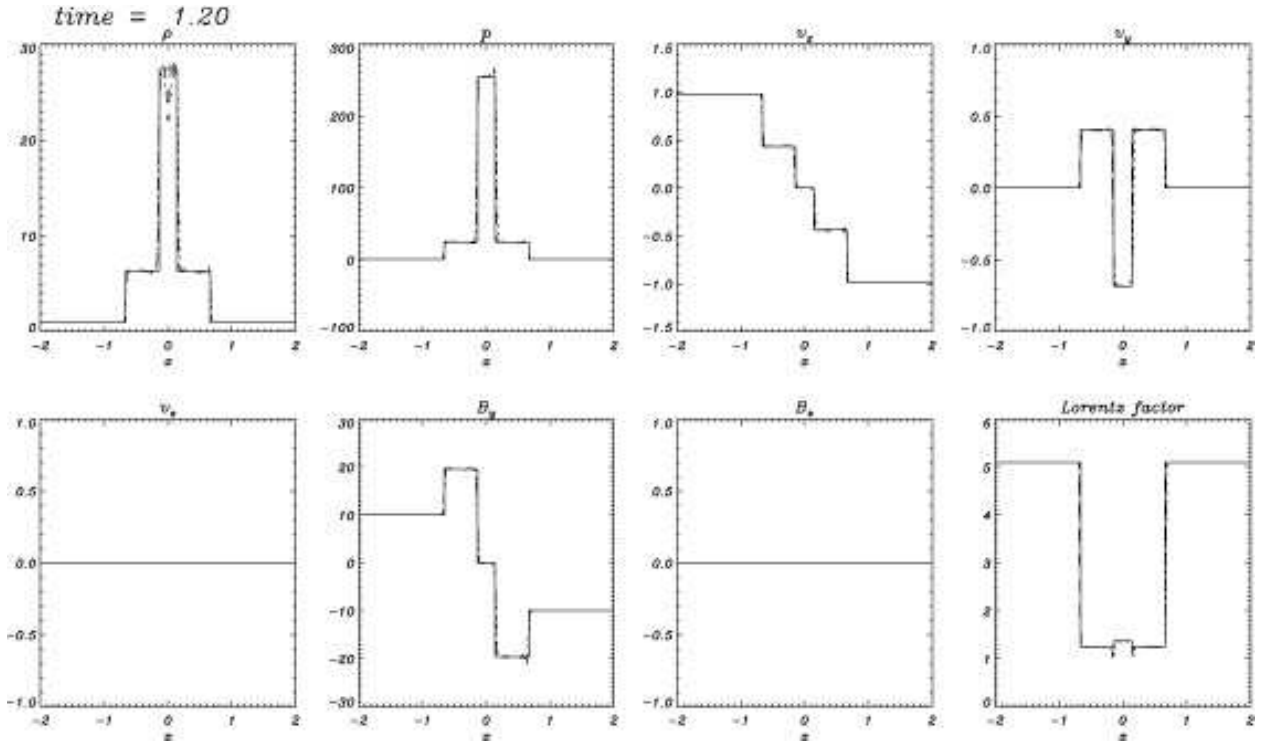


Fig. 5.— Simulation results of Komissarov collision test at time $t = 1.5$ using the CENO (dotted lines) and the PPM (dashed lines) reconstructions. The solid lines are the exact solution. The results are composed of a left-going fast shock, of a left-going slow shock, a right-going slow shock, and a right-going fast shock.

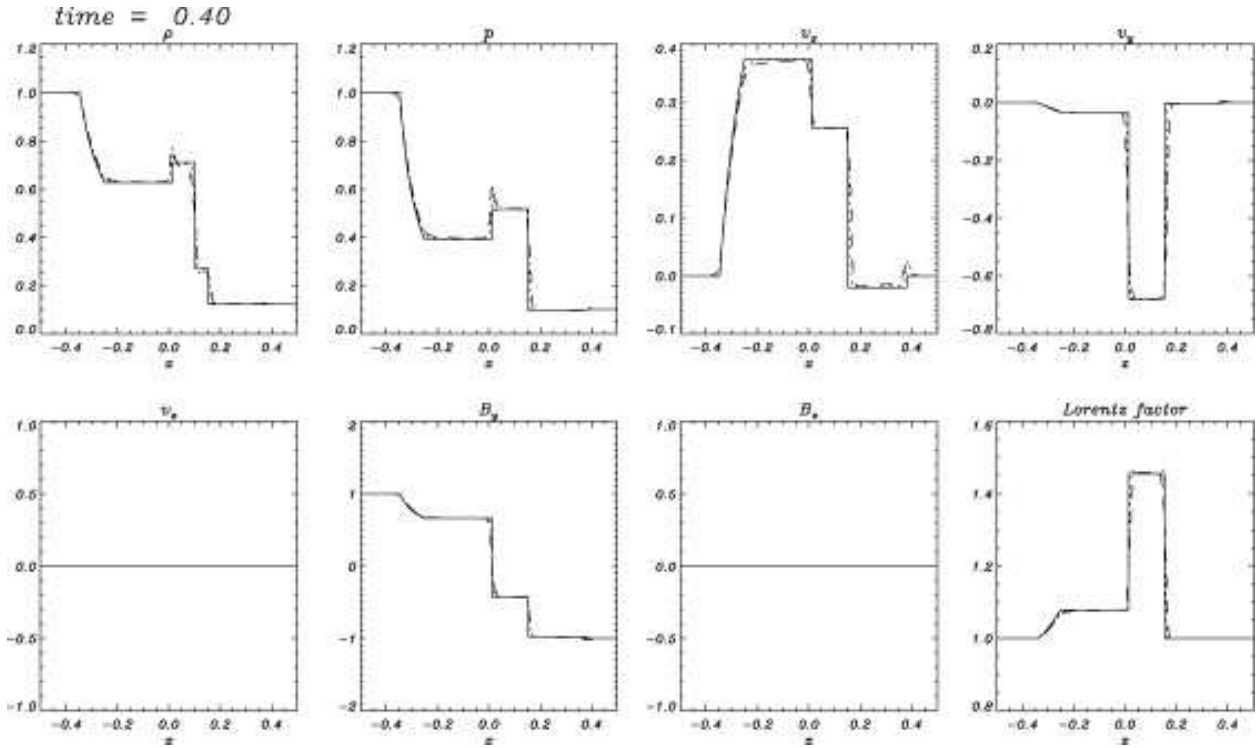


Fig. 6.— Simulation results of Balsara test 1 at time $t = 0.4$ using the MC slope limiter (dotted lines) and the minmod slope limiter (dashed lines) reconstructions. The solid lines are the exact solutions. The results are composed of a left-going fast rarefaction, of a left-going slow shock, of a contact discontinuity, of a right-going slow shock and of a right-going fast rarefaction.

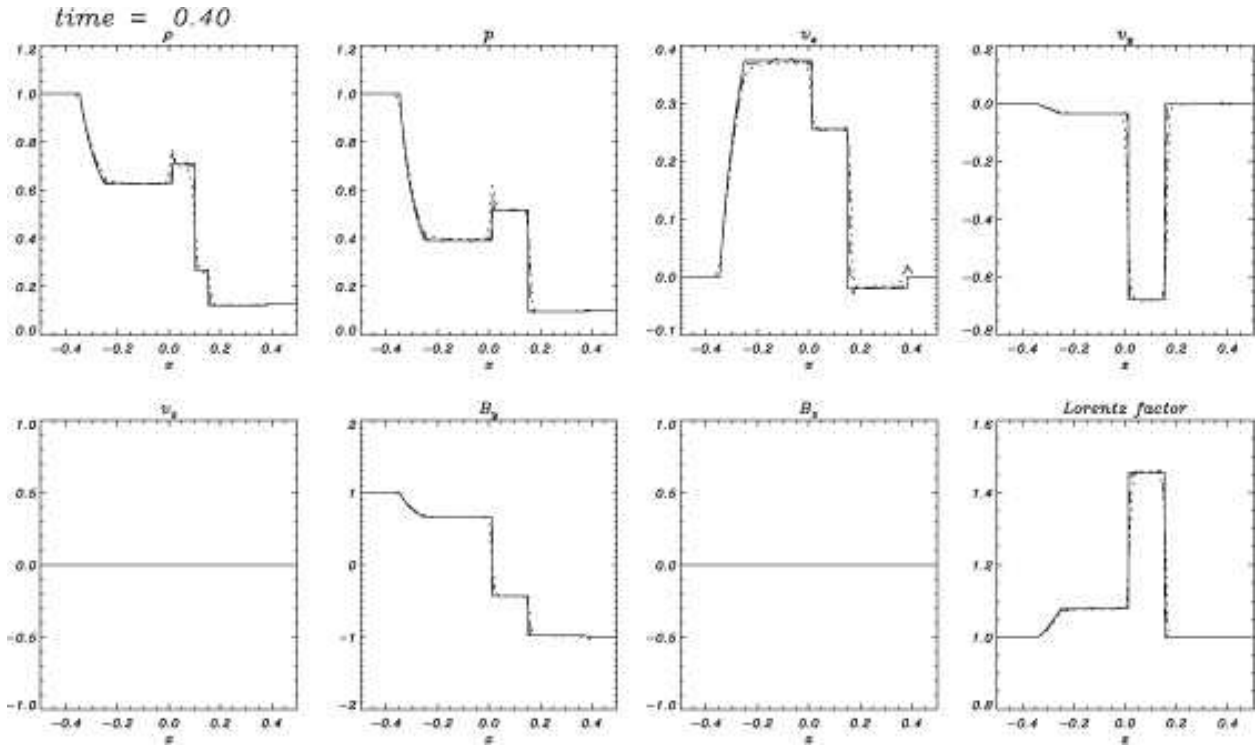


Fig. 7.— Simulation results of Balsara test 1 at time $t = 0.4$ using the CENO (dotted lines) and the PPM (dashed lines) reconstructions. The solid lines are the exact solutions. The results are composed of a left-going fast rarefaction, of a left-going slow shock, a contact discontinuity, of a right-going slow shock, and a right-going fast rarefaction.

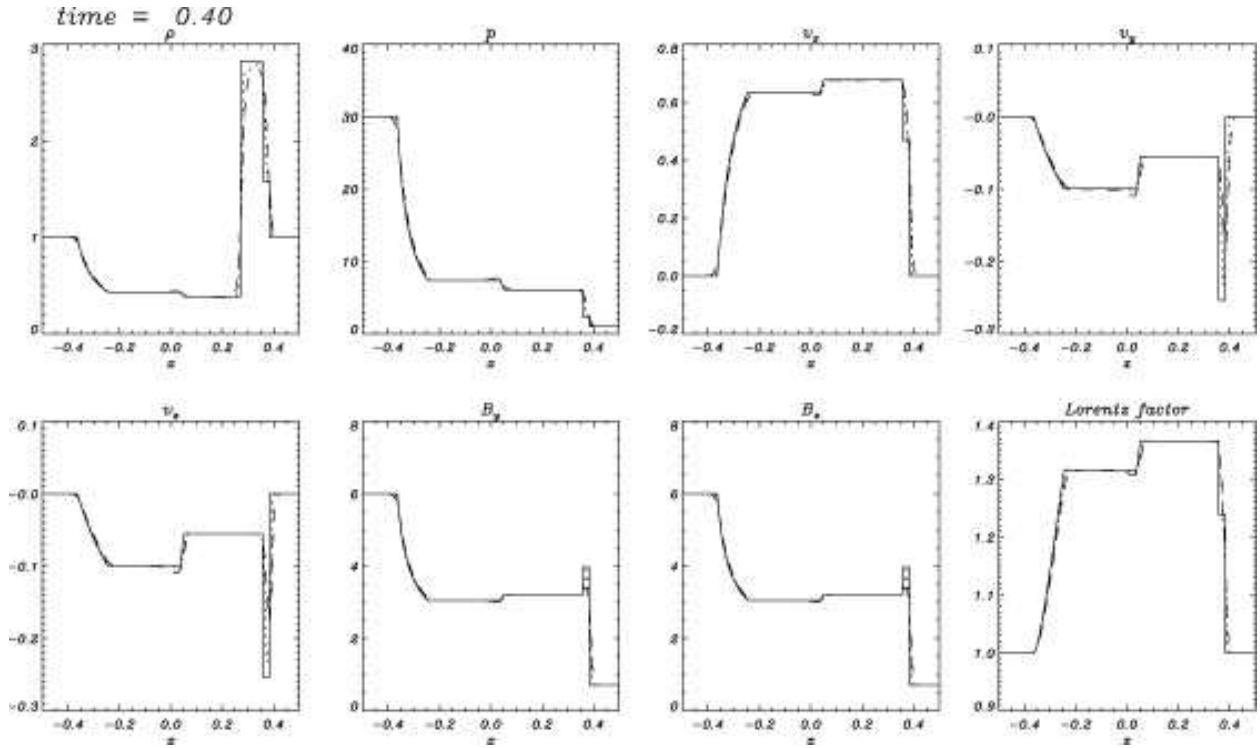


Fig. 8.— Simulation results of Balsara test 2 at time $t = 0.4$ using the MC slope limiter (dotted lines) and the minmod slope limiter (dashed lines) reconstructions. The solid lines are the exact solutions. The results are composed of two left-going fast and slow rarefactions, a contact discontinuity, and two right-going fast and slow shocks.

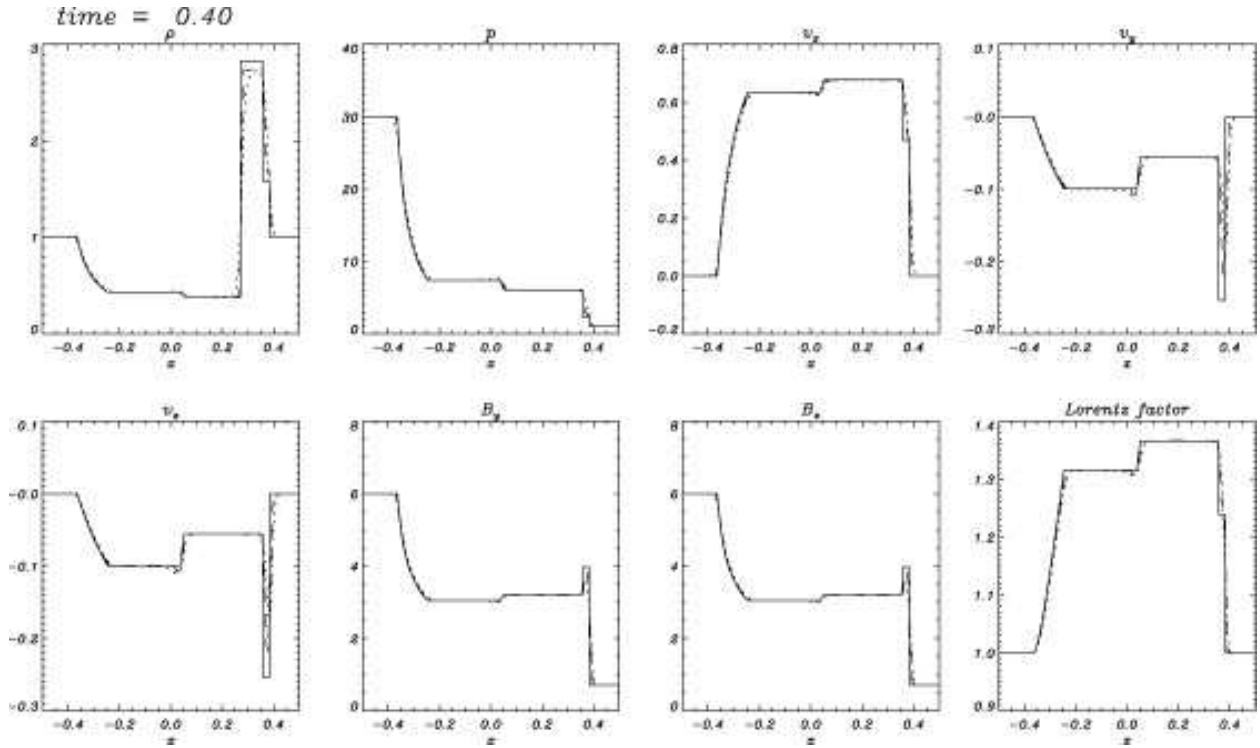


Fig. 9.— Simulation results of Balsara test 2 at time $t = 0.4$ using the CENO (dotted lines) and the PPM (dashed lines) reconstructions. The solid lines are the exact solutions. The results are composed of two left-going fast and slow rarefactions, a contact discontinuity, and two right-going fast and slow shocks.

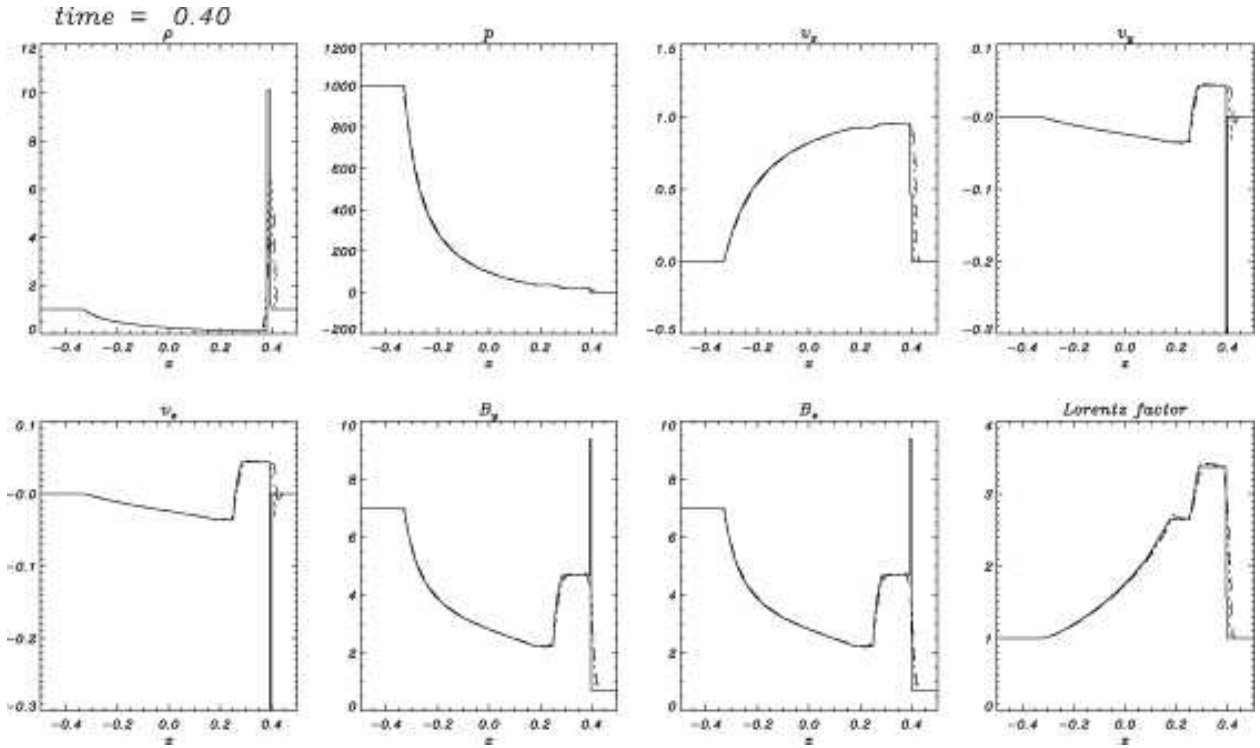


Fig. 10.— Simulation results of Balsara test 3 at time $t = 0.4$ using the MC slope limiter (dotted lines) and the minmod slope limiter (dashed lines) reconstructions. The solid lines are the exact solution. The results are composed of two left-going fast and slow rarefactions, a contact discontinuity, and two right-going fast and slow shocks.

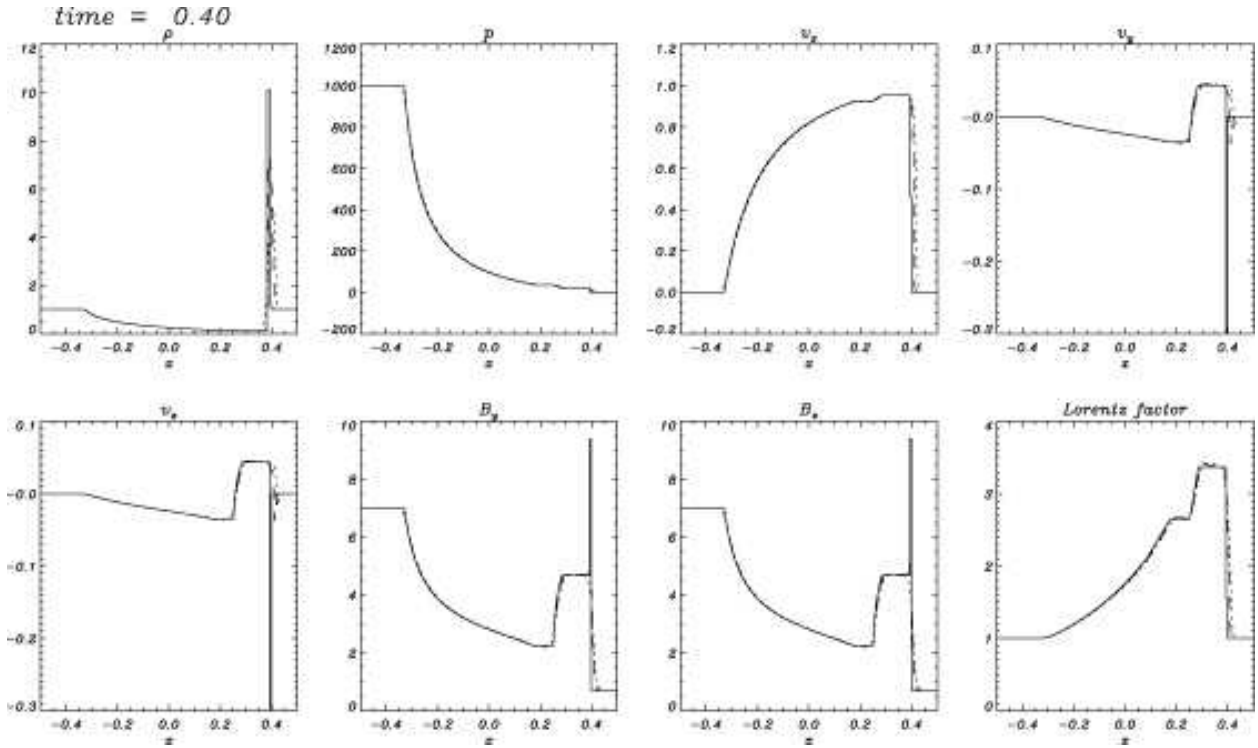


Fig. 11.— Simulation results of Balsara test 3 at time $t = 0.4$ using the CENO (dotted lines) and the PPM (dashed lines) reconstructions. The solid lines are the exact solution. The results are composed of two left-going fast and slow rarefactions, a contact discontinuity, and two right-going fast and slow shocks.

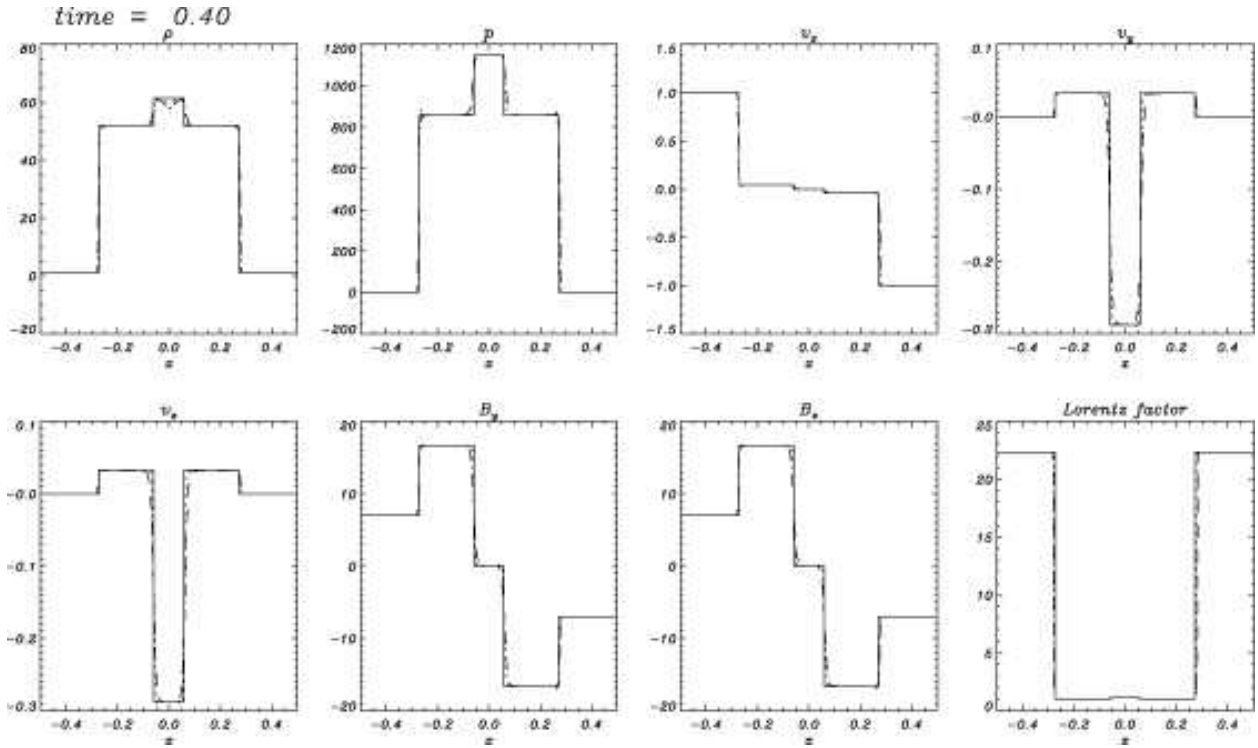


Fig. 12.— Simulation results of Balsara test 4 at time $t = 0.4$ using the MC slope limiter (dotted lines) and the minmod slope limiter (dashed lines) reconstructions. The solid lines are the exact solution. The results are composed of two left-going fast and slow shocks, and two right-going fast and slow shocks.

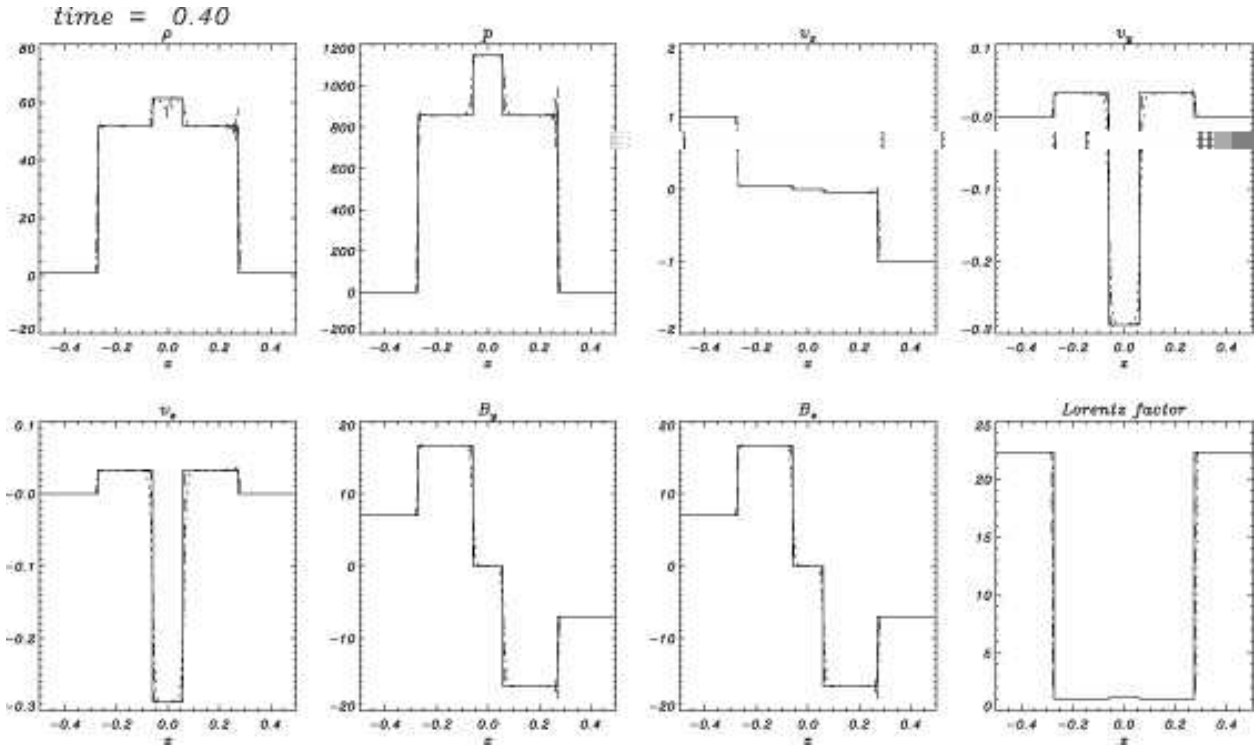


Fig. 13.— Simulation results of Balsara test 4 at time $t = 0.4$ using the CENO (dotted lines) and the PPM (dashed lines) reconstructions. The solid lines are the exact solution. The results are composed of two left-going fast and slow shocks, and two right-going fast and slow shocks.

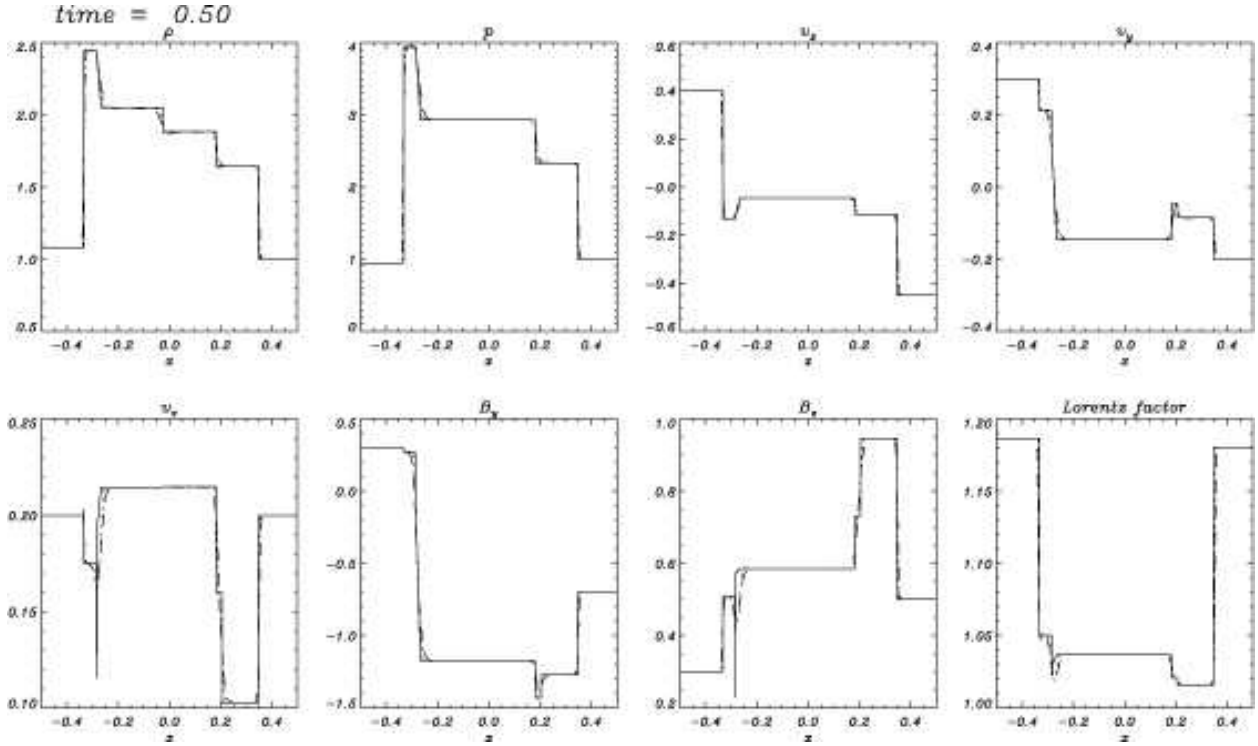


Fig. 14.— Simulation results of Balsara test 5 at time $t = 0.5$ using the MC slope limiter (dotted lines) and the minmod slope limiter (dashed lines) reconstructions. The solid lines are the exact solution. The results are composed of a left-going fast shock, a left-going Alfvén discontinuity, a left-going slow rarefaction, a contact discontinuity, a right-going slow shock, a right-going Alfvén discontinuity, and a right-going fast shock.

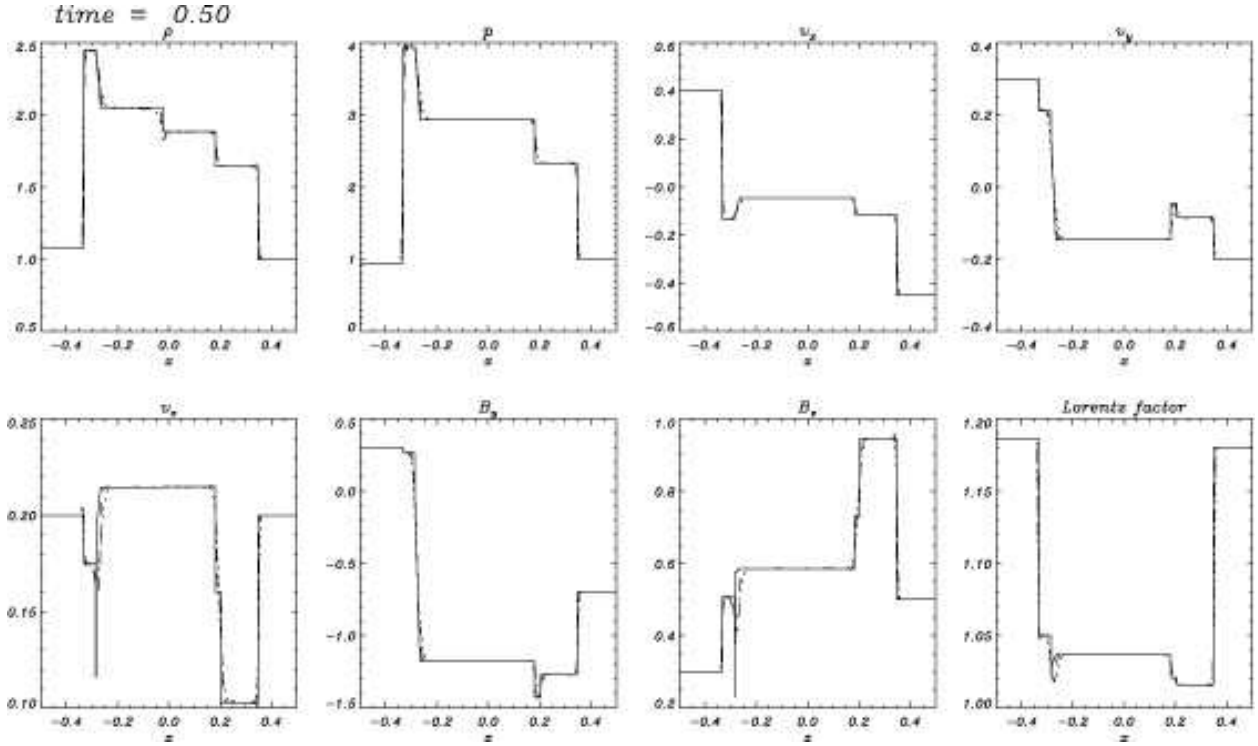


Fig. 15.— Simulation results of Balsara test 5 at time $t = 0.5$ using the CENO (dotted lines) and the PPM (dashed lines) reconstructions. The solid lines are the exact solution. The results are composed of a left-going fast shock, a left-going Alfvén discontinuity, a left-going slow rarefaction, a contact discontinuity, a right-going slow shock, a right-going Alfvén discontinuity, and a right-going fast shock.

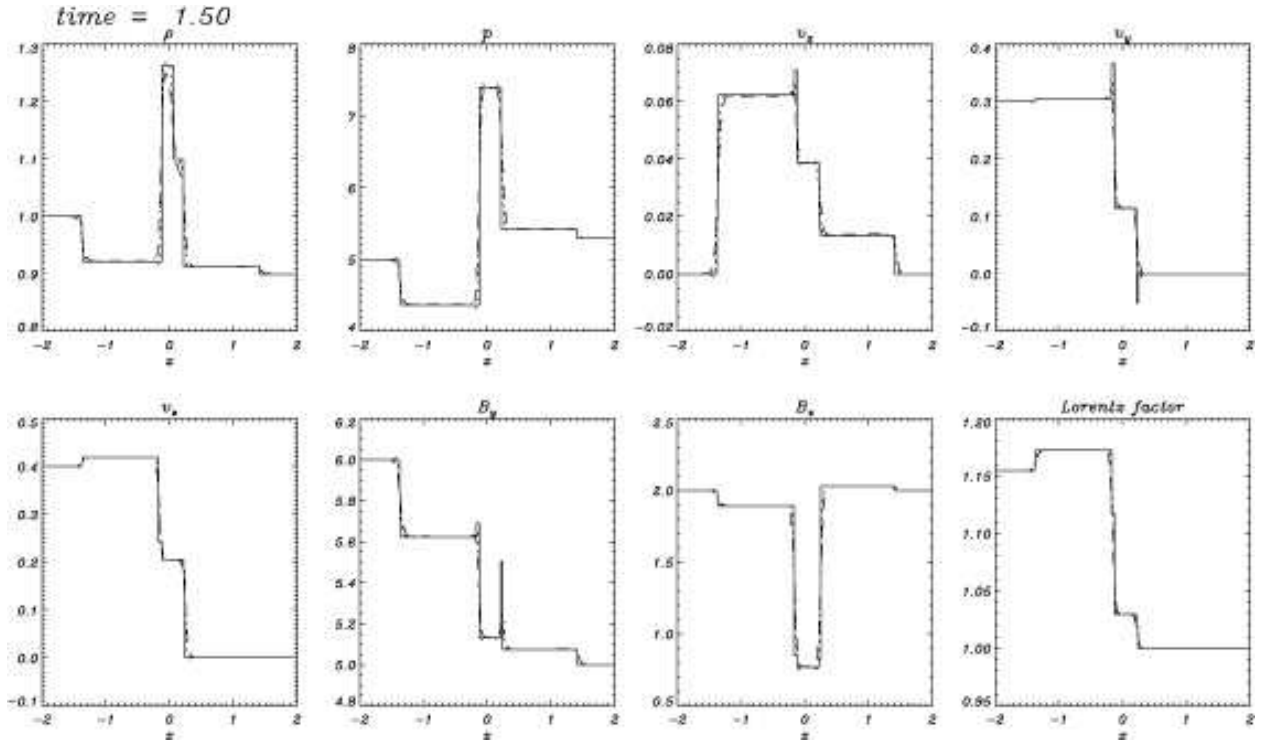


Fig. 16.— Simulation results of Generic Alfvén test at time $t = 1.5$ using the MC slope limiter (dotted lines) and the minmod slope limiter (dashed lines) reconstructions. The solid lines are the exact solution. The results are composed of a left-going fast rarefaction, a left-going Alfvén discontinuity, a left-going slow shock, a contact discontinuity, a right-going slow shock, a right-going Alfvén discontinuity, and a right-going fast shock.

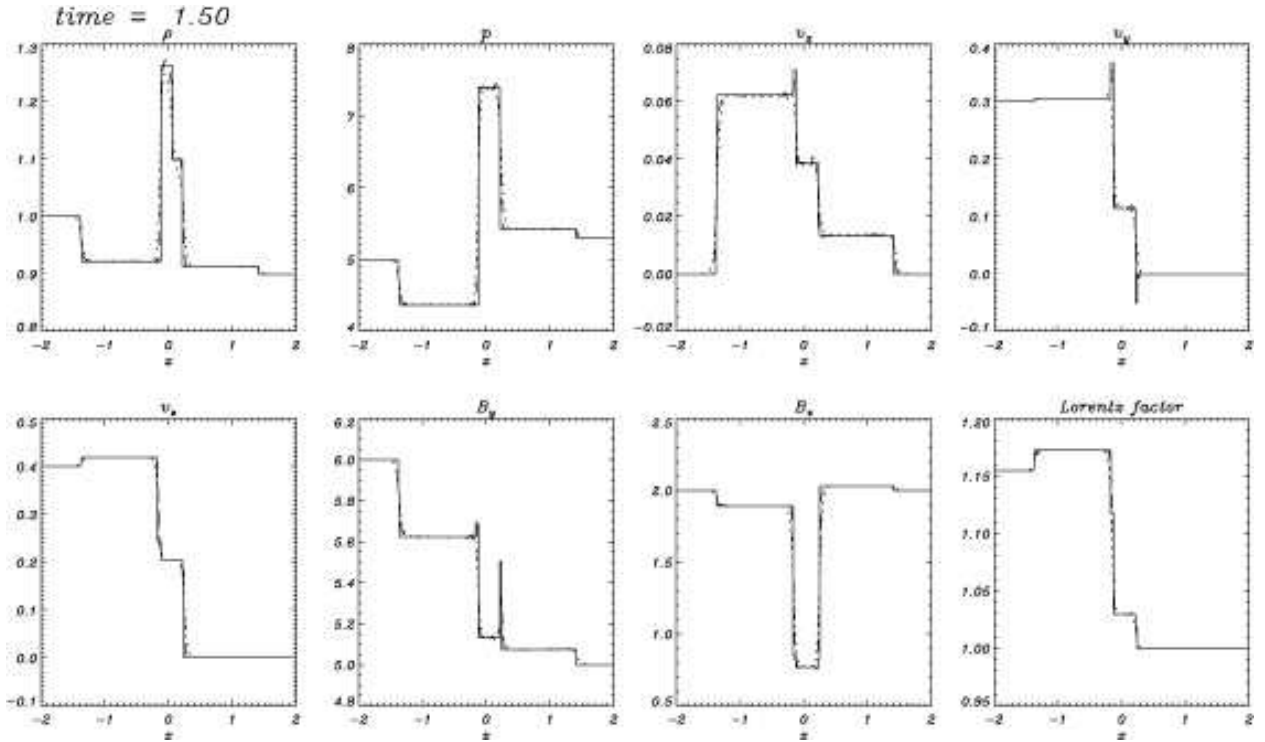


Fig. 17.— Simulation results of Generic Alfvén test at time $t = 1.5$ using the CENO (dotted lines) and the PPM (dashed lines) reconstructions. The solid lines are the exact solution. The results are composed of a left-going fast rarefaction, a left-going Alfvén discontinuity, a left-going slow shock, a contact discontinuity, a right-going slow shock, a right-going Alfvén discontinuity, and a right-going fast shock.

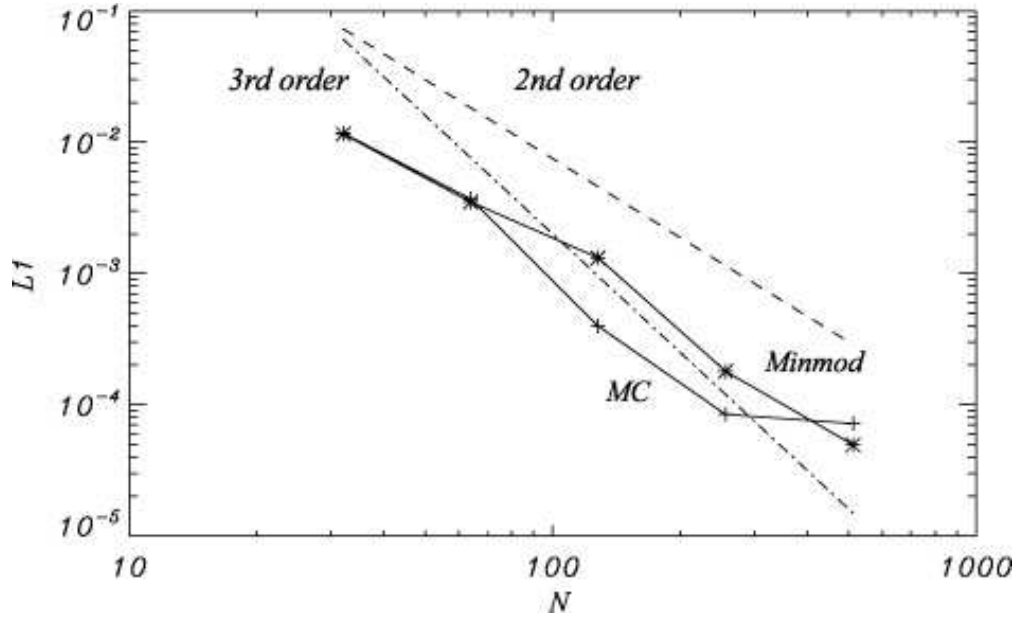


Fig. 18.— L_1 norm of the error in v^x for a magnetized Bondi accretion flow as a function of computational zone number N for the MC slope limiter (plus) and the minmod slope limiter (asterisk) reconstructions. The straight lines show the slope expected for second-order convergence (dashed line) and third-order convergence (dash-dotted line).